



## Quantification of rhenium oxide dispersion on zeolite: Effect of zeolite acidity and mesoporosity



Yiqing Wu<sup>a</sup>, Scott Holdren<sup>b</sup>, Yuan Zhang<sup>a</sup>, Su Cheun Oh<sup>a</sup>, Dat T. Tran<sup>c</sup>, Laleh Emdadi<sup>a,c</sup>, Zheng Lu<sup>d</sup>, Mei Wang<sup>a</sup>, Taylor J. Woehl<sup>a</sup>, Michael Zachariah<sup>a,b</sup>, Yu Lei<sup>d</sup>, Dongxia Liu<sup>a,\*</sup>

<sup>a</sup> Department of Chemical and Biomolecular Engineering, University of Maryland, College Park, MD 20742, USA

<sup>b</sup> Department of Chemistry and Biochemistry, University of Maryland, College Park, MD 20742, USA

<sup>c</sup> U.S. Army Research Laboratory, RDRL-SED-C, 2800 Powder Mill Road, Adelphi, MD 20783, USA

<sup>d</sup> Department of Chemical and Materials Engineering, The University of Alabama in Huntsville, 301 Sparkman Drive, Huntsville, AL 35899, USA

### ARTICLE INFO

#### Article history:

Received 2 August 2018

Revised 27 January 2019

Accepted 23 February 2019

#### Keywords:

Rhenium oxide  
Brønsted acid site  
Silanol group  
Spatial distribution  
2D lamellar zeolite  
DRIFTS  
Raman spectra

### ABSTRACT

The anchoring nature and spatial distribution of rhenium oxide (ReO<sub>x</sub>) supported on zeolites (ReO<sub>x</sub>/zeolite) were determined as a function of the support acidity and mesoporosity. The ReO<sub>x</sub>/zeolite samples were characterized collectively using Argon isotherm, XRD, Raman, XAS, DRIFTS, and organic chemical titrations. The results show that the ReO<sub>x</sub> species formed the isolated distorted tetrahedral ReO<sub>4</sub> structure. On the zeolite support, ReO<sub>x</sub> species anchored predominantly on Brønsted acid sites (Si-OH<sup>+</sup>-Al) enclosed in micropores (internal acid sites), by replacing the protons in Si-OH<sup>+</sup>-Al sites at a H<sup>+</sup>/Re ratio of ~1.1 in zeolites with high acidity. The decrease in zeolite acidity led to the anchoring of ReO<sub>x</sub> species onto both Si-OH<sup>+</sup>-Al and silanol group (Si-OH). The increase in zeolite mesoporosity migrated the ReO<sub>x</sub> species onto both internal acid sites and those on the external surface and mesopores (external acid sites), as well as Si-OH groups. The implication of distribution of ReO<sub>x</sub> in zeolite was explored by direct non-oxidative methane conversion reaction.

© 2019 Elsevier Inc. All rights reserved.

### 1. Introduction

Metal oxides supported on substrates that possess high surface areas have found various applications in heterogeneous catalysis [1,2]. The supported metal oxides are usually transition metal oxide materials, such as rhenium oxide [3,4], molybdenum oxide [5,6] and chromium oxide [7,8]; while the high surface area substrates usually include metal oxides [9–12], such as alumina, titania and zirconia, as well as zeolites [13–15]. Among all these high surface area supports, zeolites are unique due to their well-defined angstrom-sized microporous crystalline structure, which allows high dispersion of metal oxide species and is essential for enabling catalyst shape selectivity and stability. Hence, metal oxide supported on zeolite materials have been widely used as heterogeneous catalysts for a variety of reactions, including direct methane aromatization [16,17], Fischer-Tropsch process [18] and upgrading of bio-fuels [19,20].

The development of two-dimensional (2D) lamellar zeolites, consisting of both mesopores (20–500 Å) and micropores (<20 Å),

provides an opportunity to explore new catalytic properties of zeolite supported metal oxide catalysts, due to the enhanced molecular diffusion and facilitated accessibility of active sites through the connected meso- and micropore network. 2D zeolites have been synthesized by intercalation [21–25], exfoliation [26–30], pillaring [31,32], etc. of the precursor materials that contain stacked sheets of one-to-two unit cell thickness organized by weak forces through the interactions of organic/inorganic ions and/or molecules located in the “interlayer” spaces. As the characteristic length of the microporous domains in 2D zeolites approaches the single- or near single-unit-cell level, the percentage of external surface or mesopores becomes comparable to that of micropores, in contrast to the sole microporous structure in conventional 3D zeolites. Since the catalytic performance of metal oxides is sensitive to the local environment, it is essential to obtain knowledge of the anchoring nature and spatial distribution of metal oxide species in 2D micro-/mesoporous zeolites in order to understand their catalytic properties.

We have made initial efforts on understanding of spatial distribution of metal-acid active sites in molybdenum oxide loaded MFI zeolite (MoO<sub>x</sub>/MFI) catalysts, in which the zeolites have tunable meso-/microporous lamellar structures [16]. That study showed that the concentration of free Brønsted acid sites (Si-OH<sup>+</sup>-Al) increased linearly, accompanied by a linear decrease in Mo

\* Corresponding author.

E-mail address: [liud@umd.edu](mailto:liud@umd.edu) (D. Liu).

dispersion, with decreasing external surface areas in MoO<sub>x</sub>/MFI catalysts. The Mo-acid active sites coexistence on the external surface or mesopores of the catalysts linearly depended on the hierarchy factor, being the product of relative micropore volume and relative external surface area. The reaction rate and product selectivity of MoO<sub>x</sub>/MFI catalysts in direct non-oxidative methane aromatization (DNMC) reaction were consistent with the trends of changes in zeolite porosities. These results imply that a balance between the meso- and microporosity in the zeolite, and the resultant metal-acid active site distribution can be realized for maximization of catalyst performances in DNMC reactions. It should be noted that we were able to quantify the acid site concentration and spatial distribution, but not the anchoring nature and spatial location of MoO<sub>x</sub> species. MoO<sub>x</sub> species could interact with two Si-OH<sup>+</sup>-Al sites to form a (Mo<sub>2</sub>O<sub>5</sub>)<sup>2+</sup> dimer or a (MoO<sub>2</sub>)<sup>2+</sup> monomer structure [13–15,33,34]. Therefore, the replacement of the protons (H<sup>+</sup>) in Si-OH<sup>+</sup>-Al sites by MoO<sub>x</sub> (e.g., H<sup>+</sup>/Mo ratio) exists at one-to-one and two-to-one ratios. This brings the challenge in quantifying the anchoring nature and spatial distribution of MoO<sub>x</sub> sites in lamellar zeolites by simple interpretation of changes in the concentration of Si-OH<sup>+</sup>-Al sites determined by organic chemical titrations [16,35–37], which was the main technique used for quantitative evaluation on acid site concentration in our previous study.

As an analogue to MoO<sub>x</sub>, rhenium oxide (ReO<sub>x</sub>) on zeolite supports has often been investigated as catalyst for various reactions, including metathesis of olefins [38–40], benzene oxidation to phenol [41–43], dealkylation of heavy reformates into xylenes [44] and epoxidation of olefins [45]. It is expected to be an active catalyst in DNMC for methane valorization. Similarly, ReO<sub>x</sub> species anchored onto Si-OH<sup>+</sup>-Al sites in zeolites could form O<sub>2</sub>Re(μ-O<sub>2</sub>)ReO<sub>2</sub><sup>2+</sup> dimer and/or Si-O<sub>7</sub>ReO<sub>3</sub>-Al monomer structures [46,47]. The replacement of protons in Si-OH<sup>+</sup>-Al sites by ReO<sub>x</sub> in both anchoring structures, however, follows nearly a one-to-one ratio (i.e., H<sup>+</sup>/Re ratio = 1.1). On the basis of this understanding, the loss of free Si-OH<sup>+</sup>-Al sites in zeolites upon ReO<sub>x</sub> loading could reflect the quantity of ReO<sub>x</sub> on zeolites. The exploration of Si-OH<sup>+</sup>-Al site loss would indicate the spatial distribution of ReO<sub>x</sub> species in the zeolite support. In literature, studies on the anchoring structure of ReO<sub>x</sub> on zeolites have focused on the 3D zeolites with low Si/Al ratios (typically, Si/Al ratio < 20) [41,42,46,47]. With the increased focus on 2D zeolites in recent years, it should be interesting to explore the dispersion of ReO<sub>x</sub> in these new zeolite materials that have high mesoporosity and/or high Si/Al ratios.

In this work, we prepared ReO<sub>x</sub> supported on 2D pillared MFI (PMFI) and pillared MWW (PMWW) zeolites, as well as on their microporous MFI and MWW analogues, to investigate the influences of acidity and mesoporosity on the anchoring nature and spatial distribution of ReO<sub>x</sub> species. The textural properties of the ReO<sub>x</sub>/zeolite samples were characterized by Argon (Ar) isotherms. X-ray diffraction patterns (XRD), Raman spectroscopy, and X-ray absorption spectroscopy (XAS) were conducted to understand the structure of ReO<sub>x</sub> in the zeolite supports at ambient conditions. The change in the spatial distribution of acid sites and its correlation to the change of ReO<sub>x</sub> distribution were determined by organic base titrations, after the dehydration treatment of the ReO<sub>x</sub>/zeolite samples in flowing dry gas under high temperature. *In-situ* Diffuse Reflectance Infrared Fourier Transform Spectroscopy (DRIFTS) measurements support the disturbance of acid sites and silanol groups (Si-OH) in the zeolite by the loading of ReO<sub>x</sub> species. The DNMC reaction was run over the as-prepared ReO<sub>x</sub>/zeolite catalysts to study their catalytic performances. The correlation between the catalyst property and catalytic performance was developed. In combination, all these studies enabled the quantitative evaluation of anchoring nature and spatial distribution of ReO<sub>x</sub> species on zeolites with different mesoporosity/acidity and of their implication on DNMC catalytic reactions.

## 2. Experimental

### 2.1. Preparation of ReO<sub>x</sub>/zeolite catalysts

#### 2.1.1. Synthesis of zeolite materials

In order to synthesize 2D PMWW and 3D MWW zeolites, their precursor, MWW(P), was prepared. The hydrothermal synthesis of MWW(P) was carried out by using the method described by Corma et al. [30]. One portion of the MWW(P) product was dried and calcined to produce 3D MWW. The other portion of MWW(P) was swollen according to the method developed by Maheshwari et al. [32], followed by pillaring of the swollen material using the procedure reported by Barth et al. [48] to make 2D PMWW zeolite. Two batches of MWW zeolites were prepared in order to obtain samples with different acidity (i.e., Si/Al ratio of 20 and 30), which were designated as MWW-20 and MWW-30, respectively.

The 2D PMFI zeolite was prepared using the method reported by Na et al. [31]. In order to synthesize PMFI, the multilamellar MFI, as the precursor of PMFI, was synthesized following the procedure reported by Ryoo's group [49]. For comparison, we made the other lamellar MFI zeolite that has lower Si/Al ratio and mesoporosity than PMFI, but high mesoporosity than and similar Si/Al ratio to 3D MFI zeolite material. This sample was synthesized via a dual template method reported by Emdadi et al. [50], which employed [C<sub>22</sub>H<sub>45</sub>-N<sup>+</sup>(CH<sub>3</sub>)<sub>2</sub>-C<sub>6</sub>H<sub>12</sub>-N<sup>+</sup>(CH<sub>3</sub>)<sub>2</sub>-C<sub>6</sub>H<sub>13</sub>](Br<sup>-</sup>)<sub>2</sub> (C<sub>22-6-6</sub>) and tetrapropylammonium hydroxide (TPAOH) at the C<sub>22-6-6</sub>/TPAOH molar ratio of 10/5. The obtained zeolite sample was defined as MFI-10/5. Commercial MFI with Si/Al of 40 (MFI-40, Stock No. 45880) and Si/Al of 15 (MFI-15, Stock No. 45882) were purchased from Alfa Aesar, and used as representatives of 3D MFI zeolites with different acidity in this study.

The as-synthesized PMWW, MWW-20, MWW-30, PMFI and MFI-10/5 zeolites were ion-exchanged three times using 1 M aqueous ammonium nitrate (NH<sub>4</sub>NO<sub>3</sub>) (weight ratio of zeolite to NH<sub>4</sub>NO<sub>3</sub> solution = 1:10) at 353 K for 12 h, and subsequently, collected by vacuum filtration, washed with deionized (DI) water three times, and dried at 343 K overnight. The MFI-40 and MFI-15 were purchased in the NH<sub>4</sub><sup>+</sup>-form. All zeolite samples in their NH<sub>4</sub><sup>+</sup>-form were treated in dry air (1.667 mL s<sup>-1</sup>, breathing grade, Airgas) by increasing the temperature from 298 K to 823 K at 0.03 K s<sup>-1</sup> and holding for 4 h to thermally decompose NH<sub>4</sub><sup>+</sup> to NH<sub>3</sub> and H<sup>+</sup>.

#### 2.1.2. Preparation of ReO<sub>x</sub>/zeolite samples

The wetness impregnation method was used to prepare the ReO<sub>x</sub>/zeolite samples. In the synthesis, 0.0758 g of ammonium perchlorate (NH<sub>4</sub>ReO<sub>4</sub>, greater than 99% purity, Sigma-Aldrich) was dissolved in 0.5 g deionized (DI) water at 343 K to form a solution, which was then quickly added dropwise to 1.0 g zeolite. The as-prepared ReO<sub>x</sub>/zeolite catalyst was dried at 393 K overnight, followed by a 10 h calcination at 773 K under air flow (1.667 mL s<sup>-1</sup>). For simplicity, Re loaded MFI-15, MFI-40, MFI-10/5, PMFI, MWW-20, MWW-30 and PMWW, were designated as Re/MFI-15, Re/MFI-40, Re/MFI-10/5, Re/PMFI, Re/MWW-20, Re/MWW-30 and Re/PMWW, respectively. For comparison, ReO<sub>x</sub> species were loaded onto silica support to form Re/SiO<sub>2</sub> catalysts. The synthesis procedure was the same as that of ReO<sub>x</sub>/zeolite samples, except that zeolite support was replaced with silica (fume silica, Sigma-Aldrich). In the synthesis, the added ReO<sub>x</sub> precursor was supposed to transform into 5 wt% Re loading in each catalyst sample.

### 2.2. ReO<sub>x</sub>/zeolite characterization

The Si and Al compositions of the zeolite samples were determined by inductively coupled plasma optical emission spec-

troscopy (ICP-OES, Thermo Fisher Scientific iCAP 6500), while Re composition was determined by inductively coupled plasma mass spectroscopy (ICP-MS, Thermo Fisher Scientific XSERIES 2). The crystalline phases of the  $\text{ReO}_x/\text{zeolite}$  samples were examined by the powder XRD using a Rigaku Ultima III instrument with  $\text{Cu-K}\alpha$  radiation. Ar adsorption-desorption isotherms were measured at 87 K with an Autosorb-iQ analyzer (Quantachrome Instruments) to characterize the textural properties of the zeolite samples, before and after  $\text{ReO}_x$  loading, respectively. Prior to the measurement, all the samples were evacuated overnight at 623 K and 1 mm Hg. The structure of the  $\text{ReO}_x$  species in zeolites was determined by Raman spectra, which were collected using a Renishaw Raman microscope. The XAS measurement was conducted to understand the coordination structure of  $\text{ReO}_x$  in zeolites under ambient conditions.  $\text{Re L}_I$  and  $\text{L}_{III}$  edge XAS measurements of the  $\text{ReO}_x/\text{zeolite}$  samples were conducted at beamline 10- and 5-BM-D at the Advanced Photon Source in Argonne National Laboratory. The XAS data were recorded under fluorescence mode. Re foil,  $\text{ReO}_2$ ,  $\text{ReO}_3$  and  $\text{NH}_4\text{ReO}_4$  were used as references and measured at the same beamlines. The X-ray absorption near edge structure (XANES) and extended X-Ray absorption fine structure (EXAFS) parts of the XAS data were analyzed using Athena and Artemis softwares, respectively.

### 2.3. Acidity determination

The concentration of Brønsted acid sites in the zeolite samples (i.e.,  $N_{\text{total, H}}^+$ ), prior to and after  $\text{ReO}_x$  loading, respectively, was measured via the dimethyl ether (DME) titration, given that the Brønsted acid sites participate in reactions of DME with  $\text{H}^+$  to form surface methyl groups,  $\text{CH}_3\text{OCH}_3 + 2[\text{SiO}(\text{H})\text{Al}] = 2[\text{SiO}(\text{CH}_3)\text{Al}] + \text{H}_2\text{O}$ . The experiments were carried out in a tubular packed-bed quartz reactor (10 mm inner diameter) under atmospheric pressure. The temperature of the reactor was held constant by a resistively heated furnace (National Electric Furnace FA120 type) where the temperature was controlled by a Watlow Controller (96 series). Catalyst temperatures were measured using a K-type thermocouple touching the bottom of a well on the external surface of the quartz reactor. Details on the DME titration experimental setup and reaction conditions were described in our previous publications [16,17]. The same setup was used for the following organic base titration during methanol dehydration experiment.

To study the percentage of external Brønsted acid sites (i.e., acid sites resided in mesopores and on external surface of zeolite samples,  $f_{\text{ext, H}}^+$ ), methanol ( $\text{CH}_3\text{OH}$ ) dehydration to DME in the presence of 2,6-di-tert butylpyridine (DTBP) organic base was measured at differential conversions (<2%) at 433 K. Liquid mixture of methanol (Fisher Scientific, 99.9%) and DTBP (Alfa, 98% purity) was introduced into a flowing He stream using a syringe pump (NE 1000, New Era Pump System Inc.). The reactor effluent was sent via heated transfer lines to a mass spectrometer (MS, Ametek Proline). The methanol dehydration rate was measured as DTBP titrant was continuously added until it reached a plateau. The loss in methanol reaction rate reflects the degree of accessibility of bulky DTBP molecules to Brønsted acid sites in zeolites, and hence, the percentage of external Brønsted acid sites in each zeolite was determined. The concentration of external active sites ( $N_{\text{ext, H}}^+$ ) accessible to DTBP was calculated from the product of  $f_{\text{ext, H}}^+$  and the concentration of acid sites determined by DME titration. The difference between the concentration of external acid sites and the acid sites determined by DME titration is the concentration of internal acid sites ( $N_{\text{int, H}}^+$ ) in each sample. Details on the method used for external and internal acid site determination can be referred to our previous work [37,51,52].

### 2.4. DRIFTS measurement

In order to determine the anchoring sites of Re species in zeolites, the DRIFTS technique was used to explore the change of Brønsted acid sites ( $\text{Si-OH}^+-\text{Al}$ ), silanol groups ( $\text{Si-OH}$ ) and extra-framework acid sites ( $\text{Al-OH}$ ) before and after Re loading. The DRIFTS spectra were collected using 100 scans at  $4\text{ cm}^{-1}$  resolution on a Nicolet iS-50R spectrometer equipped with a liquid  $\text{N}_2$  cooled MCT-A detector (Thermo Fisher Scientific). In a typical experiment, a desired amount of the zeolite sample is placed into the sample cell and flattened the rim of the cell, which is heated in a high temperature reaction chamber (HVC-DRP-5, Harrick Scientific) to 773 K at  $0.167\text{ K s}^{-1}$  for 1 h under flowing  $\text{Ar/O}_2$  mixture (10 mol %  $\text{O}_2$ ) when DRIFTS spectra were collected.

### 2.5. Direct non-oxidative methane conversion reaction

The DNMC reaction was conducted to study the catalytic performance of the  $\text{ReO}_x/\text{zeolite}$  catalysts. The reaction was started by heating the catalyst (0.30 g) from ambient temperature in He flow ( $50\text{ mL min}^{-1}$ ) to 953 K at ramp rate  $0.167\text{ K s}^{-1}$  under atmospheric pressure. After temperature of catalysts reached 953 K, the DNMC reaction was initiated by introducing methane into the catalyst at a flow rate of  $8.0\text{ mL min}^{-1}$  and  $\text{N}_2$  of  $2.0\text{ mL min}^{-1}$  as internal standard. The transfer lines were maintained at temperatures greater than 423 K by resistive heating to prevent product condensation. The effluents from the reaction were analyzed using the gas chromatograph (Agilent 7890 A GC) equipped with a methyl-siloxane capillary column (HP-1,  $50.0\text{ m} \times 320\text{ }\mu\text{m} \times 0.52\text{ }\mu\text{m}$ ) connected to a flame ionization detector (FID) and a packed column (ShinCarbon ST Columns, 80/100 mesh, 6 feet) connected to a thermal conductivity detector (TCD).

## 3. Results and discussion

### 3.1. Textural properties of $\text{ReO}_x/\text{zeolite}$ samples

Two zeolite framework types, MFI and MWW, were used as the supports for  $\text{ReO}_x$  species in the prepared  $\text{ReO}_x/\text{zeolite}$  catalysts. The MFI zeolite is microporous, and consists of two interconnected 10-MR channel systems: one is straight running along the b-axis direction ( $0.53 \times 0.56\text{ nm}$ ) and the other is zigzag running parallel to the a-axis direction ( $0.51 \times 0.55\text{ nm}$ ). The different acidity (or Si/Al ratio) in MFI zeolite does not affect its structural properties, which suggests that MFI-15 and MFI-40 have similar topological structures. Different from MFI-15 and MFI-40, the PMFI contains mesopores created by the inorganic pillar species sitting between MFI layers, parallel to the zigzag channels and perpendicular to the straight channels within the layers. It should be noted that the microporous MFI layers in PMFI are expected to have a long range ordering, as characterized in our previous studies [53,54]. The structure of MFI-10/5 stays between MFI-15 (and MFI-40) and PMFI since it has MFI lamellar layers, but some of the layers collapse to lose the long range ordering. Therefore, it acts as a structure transition from microporous MFI to the pillared PMFI zeolite support.

Different from the inter-connected micropore channels in MFI zeolite, MWW structure contains two independent micropore systems. One system is defined by sinusoidal 10-MR channels with dimensions of  $0.41 \times 0.51\text{ nm}$  and the other system consists of supercages delimited by 12-MR channels with dimensions of  $0.71 \times 0.71 \times 1.81\text{ nm}$ . The consecutive supercages are connected through slightly distorted elliptical 10-MR windows ( $0.40 \times 0.55\text{ nm}$ ). Both MWW-20 and MWW-30 have similar

topological structures. The PMWW was created by pillaring the MWW layers by  $\text{SiO}_2$ , containing the 10-MR sinusoidal channels and hourglass shaped pores (half of the supercages in MWW) within the intact layers and mesopores between the layers. It should be noted that the 10-MR micropore and mesopore in PMWW do not have direct communication. Also, the pillaring of MWW leads to loss of one 10-MR micropore channel.

Fig. 1 shows the Ar adsorption-desorption isotherms of zeolite and  $\text{ReO}_x$ /zeolite samples. For direct comparison, the Ar isotherms of zeolite samples before and after  $\text{ReO}_x$  loading, respectively, were plotted in the same figure. At low relative pressure range (i.e.,  $P/P_0 < 0.05$ , Fig. 1(A-C)), all MFI samples show similar Ar uptake, indicating that they have very similar microporosity due to the same type of zeolite framework. At high relative pressure (i.e.,  $0.4 < P/P_0 < 1$ ), the presence of a hysteresis loop in MFI-10/5 and PMFI zeolites (Fig. 1(C)) indicates capillary condensation due to presence of mesopores, while microporous MFI-15 (Fig. 1(A)) and MFI-40 (Fig. 1(B)) zeolites do not have these characteristics. Similar to the MFI-type zeolites, the MWW-type zeolites (Fig. 1(D)-(F)) have similar Ar uptake in the relative pressure range of  $P/P_0 < 0.05$ . The presence of hysteresis loop in the PMWW isotherm (Fig. 1(F)) reflects the mesoporosity in this sample, in comparison with its microporous counterparts, MWW-20 (Fig. 1(D)) and MWW-30 (Fig. 1(E)) zeolites. The loading of  $\text{ReO}_x$  species resulted in a slight decrease in the Ar uptake in each sample, as indicated in Fig. 1. The adsorption-desorption behavior of each  $\text{ReO}_x$ /zeolite sample, however, is kept almost the same as the bare zeolite prior to  $\text{ReO}_x$  loading.

Fig. 2 shows the pore size distributions of MFI- (Fig. 2(A)-(C)) and MWW-type (Fig. 2(D)-(F)) zeolites and  $\text{ReO}_x$ /zeolite samples. The pore size distributions were calculated from the adsorption branches of Ar isotherms by a non-local density functional theory (NLDFT) method, assuming an equilibrium kernel for cylindrical pores of siliceous zeolite. The microporous MFI-15 (Fig. 2(A)) and MFI-40 (Fig. 2(B)) have a peak centered at  $\sim 0.49$  nm, corresponding to the micropores in MFI framework. In Fig. 2(C), PMFI has both micropore and mesopore peaks at  $\sim 0.49$  nm and  $\sim 4.1$  nm, respectively. Besides the micropore peak, MFI-10/5 has a broad mesopore peak ranging from 4 to 18 nm. The difference in the shape and range of mesopore peaks of PMFI and MFI-10/5 reflects the different mesopore features and/or connectivity between mesoporous channels as reported in our recent study [55], which can be ascribed to the different formation mechanism, i.e. pillaring for PMFI [31] and dual-template assisted growth for MFI-10/5 [50]. For MWW-type samples, the microporous MWW-20 (Fig. 2(D)) and MWW-30 (Fig. 2(E)) have the micropore peak at  $\sim 0.52$  nm, while PMWW (Fig. 2(F)) has both micropore and mesopore peaks at  $\sim 0.52$  nm and  $\sim 2.7$  nm, respectively.

The loading of  $\text{ReO}_x$  into zeolites led to a slight decrease in the micropore peak of microporous MFI and MWW zeolites. For 2D lamellar PMFI, MFI-10/5 and PMWW, both micropore and mesopore peaks were decreased after  $\text{ReO}_x$  loading. These results indicate the  $\text{ReO}_x$  species are present in both micro- and mesopores of zeolite supports. Tables 1 and 2 summarize the textural properties of studied zeolites and  $\text{ReO}_x$ /zeolite samples. The 2D lamellar zeolites, including MFI-10/5, PMFI and PMWW, have hierarchical

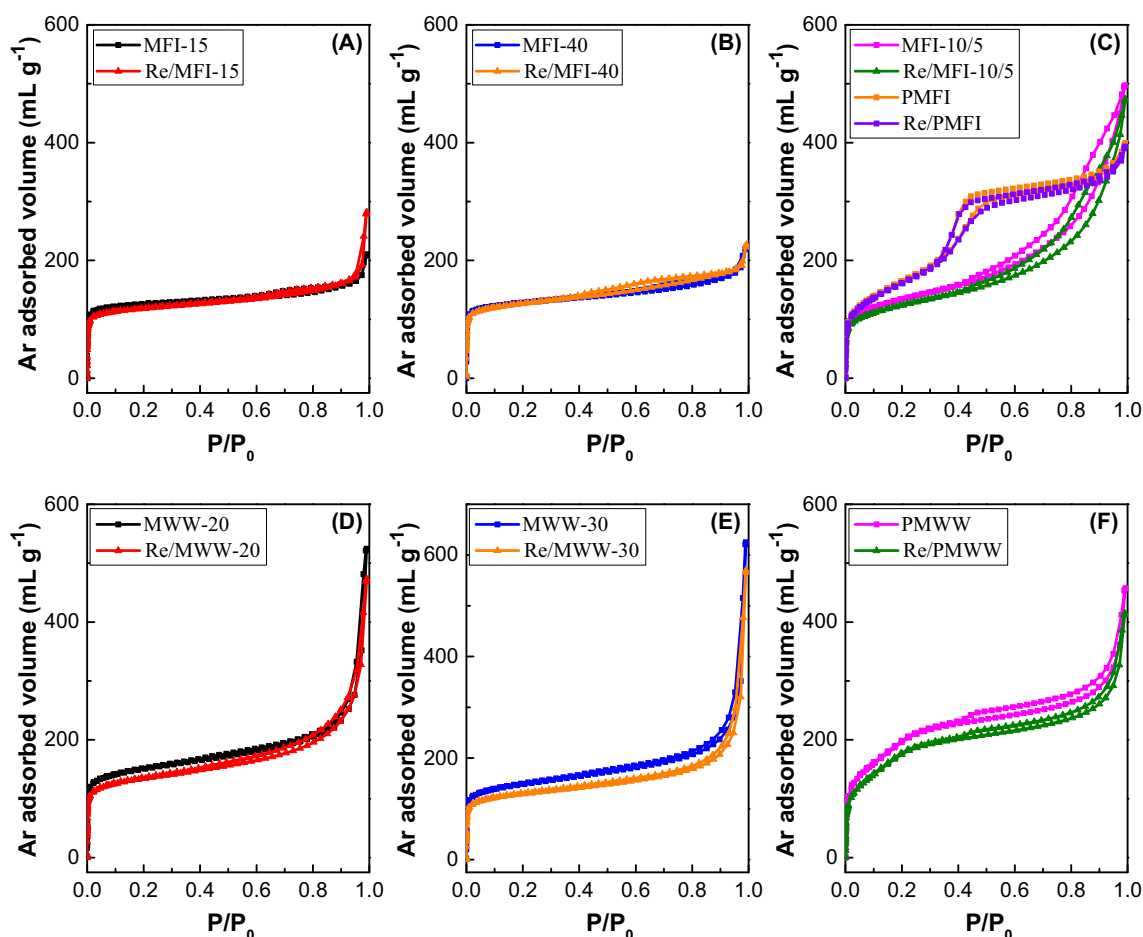
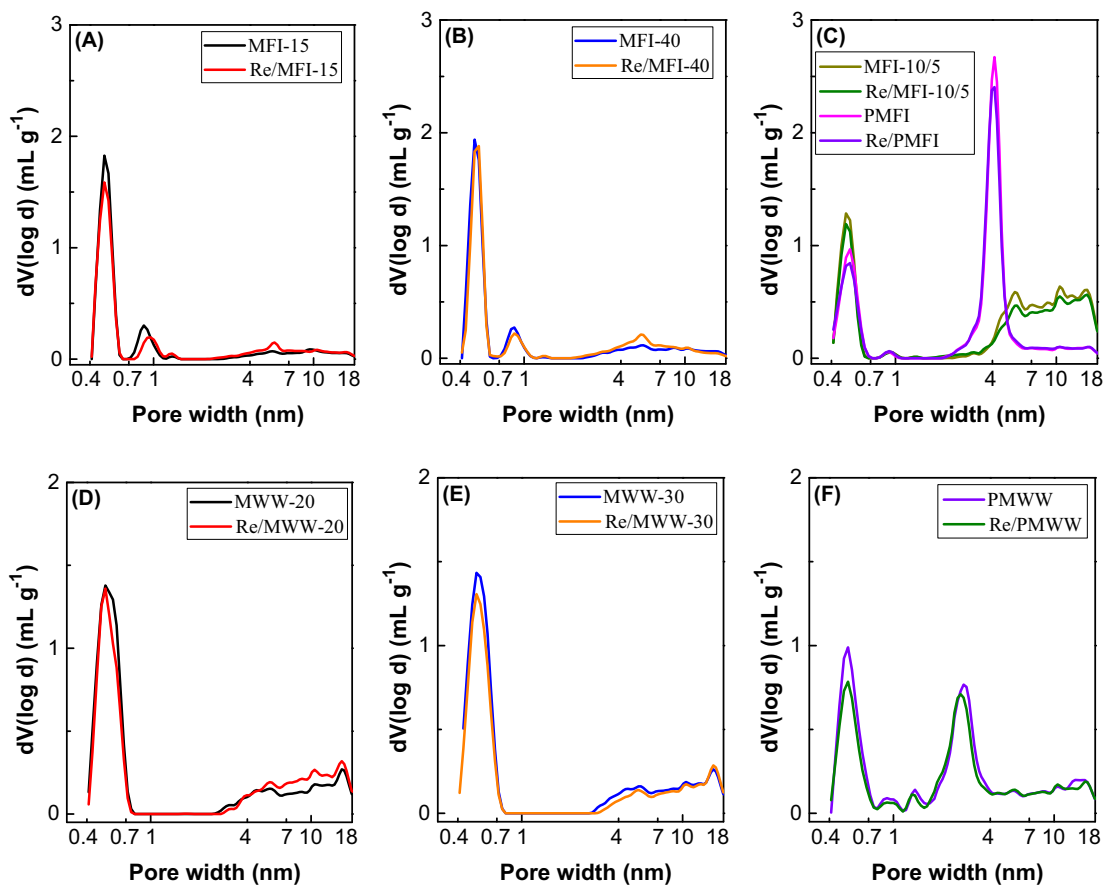


Fig. 1. Ar adsorption-desorption isotherms of MFI-15 (A), MFI-40 (B), MFI-10/5 and PMFI (C), MWW-20 (D), MWW-30 (E) and PMWW (F) before and after  $\text{ReO}_x$  loading, respectively.



**Fig. 2.** NLDFT pore size distributions of MFI-15 (A), MFI-40 (B), MFI-10/5 and PMFI (C), MWW-20 (D), MWW-30 (E) and PMWW (F), respectively, before and after  $\text{ReO}_x$  loading. The data were extracted from the adsorption branches of their Ar isotherms.

meso-/microporosity, and thus higher Brunauer–Emmett–Teller (BET) surface areas ( $S_{\text{BET}}$ ), external surface areas ( $S_{\text{ext}}$ ), mesopore volumes ( $V_{\text{meso}}$ ) and total pore volumes ( $V_{\text{total}}$ ) than their microporous counterparts. The loading of  $\text{ReO}_x$  species decreased these surface areas and pore volumes of each corresponding zeolite sample, suggesting the existence of  $\text{ReO}_x$  species in both micro- and mesopores of  $\text{ReO}_x/\text{zeolite}$  samples.

### 3.2. Structure of $\text{ReO}_x$ species in zeolite supports

When  $\text{ReO}_x/\text{zeolite}$  samples were prepared, calcination at 773 K under flowing air was employed to convert  $\text{NH}_4\text{ReO}_4$  into  $\text{ReO}_x$  species. In order to verify the crystal structure of  $\text{ReO}_x$  and change of zeolite crystallinity upon  $\text{ReO}_x$  loading, XRD mea-

surements were carried out on both zeolite and  $\text{ReO}_x/\text{zeolite}$  samples. As shown in Fig. 3, the characteristic peaks of MFI- (Fig. 3 (A)) and MWW-type (Fig. 3(B)) zeolites remained intact after the  $\text{ReO}_x$  loading. It is worth noting that the XRD patterns of 2D zeolites show less resolved characteristic peaks compared to their 3D microporous counterparts, due to the ultra-small crystal sizes (close to single-unit length), albeit they share the same microporous structures as reported in previous studies [32,49,51]. The peaks associated with  $\text{ReO}_x$  crystallite were not observed, indicating that either  $\text{ReO}_x$  formed isolated species or the size of  $\text{ReO}_x$  crystallite was too small to be detected in the studied zeolite supports. Overall, the XRD data suggests that  $\text{ReO}_x$  species had a high dispersion in the prepared  $\text{ReO}_x/\text{zeolite}$  samples.

**Table 1**

Textual properties of zeolite samples determined from Ar isotherms.

Zeolite	$S_{\text{BET}}^a$ ( $\text{m}^2 \text{g}^{-1}$ )	$S_{\text{ext}}^b$ ( $\text{m}^2 \text{g}^{-1}$ )	$S_{\text{micro}}^b$ ( $\text{m}^2 \text{g}^{-1}$ )	$V_{\text{total}}^c$ ( $\text{cm}^3 \text{g}^{-1}$ )	$V_{\text{meso}}^d$ ( $\text{cm}^3 \text{g}^{-1}$ )	$V_{\text{micro}}^e$ ( $\text{cm}^3 \text{g}^{-1}$ )
MFI-15	431	63	368	0.210	0.078	0.132
MFI-40	434	95	339	0.228	0.107	0.121
MFI-10/5	423	282	141	0.513	0.440	0.073
PMFI	519	383	136	0.456	0.395	0.061
MWW-20	493	151	342	0.352	0.227	0.125
MWW-30	486	158	328	0.356	0.236	0.120
PMWW	645	435	210	0.411	0.355	0.056

<sup>a</sup> Calculated from multi-point Brunauer–Emmett–Teller (BET) method.

<sup>b</sup> Calculated from  $t$ -plot method.

<sup>c</sup> Calculated from the adsorption branch at  $P/P_0 = 0.95$ .

<sup>d</sup>  $V_{\text{meso}} = V_{\text{total}} - V_{\text{micro}}$ .

<sup>e</sup> Determined from the cumulative micropore volume curve.

**Table 2**  
Textual properties of  $\text{ReO}_x$  loaded zeolite samples determined from Ar isotherms.

Re/Zeilite	$S_{\text{BET}}^a$ ( $\text{m}^2 \text{g}^{-1}$ )	$S_{\text{ext}}^b$ ( $\text{m}^2 \text{g}^{-1}$ )	$S_{\text{micro}}^b$ ( $\text{m}^2 \text{g}^{-1}$ )	$V_{\text{total}}^c$ ( $\text{cm}^3 \text{g}^{-1}$ )	$V_{\text{meso}}^d$ ( $\text{cm}^3 \text{g}^{-1}$ )	$V_{\text{micro}}^e$ ( $\text{cm}^3 \text{g}^{-1}$ )
Re/MFI-15	401	83	318	0.218	0.104	0.114
Re/MFI-40	421	116	305	0.234	0.124	0.110
Re/MFI-10/5	390	255	135	0.469	0.402	0.067
Re/PMFI	505	372	133	0.447	0.390	0.057
Re/MWW-20	439	143	296	0.352	0.244	0.108
Re/MWW-30	425	125	301	0.318	0.208	0.110
Re/PMWW	581	383	198	0.372	0.325	0.047

<sup>a</sup> Calculated from multi-point BET method.

<sup>b</sup> Calculated from t-plot method.

<sup>c</sup> Calculated from the adsorption branch at  $P/P_0 = 0.95$ .

<sup>d</sup>  $V_{\text{meso}} = V_{\text{total}} - V_{\text{micro}}$ .

<sup>e</sup> Determined from cumulative micropore volume curve.

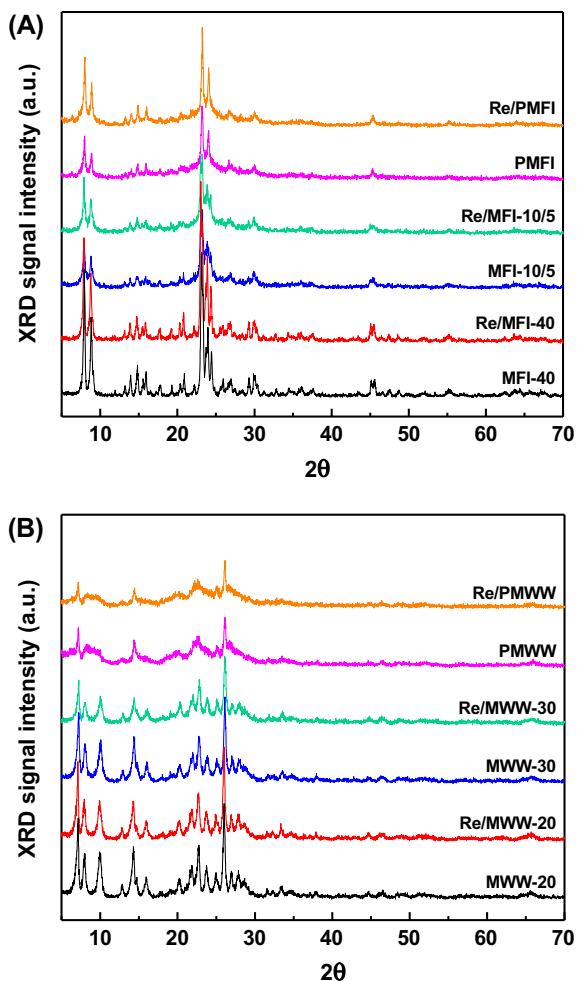


**Fig. 3.** XRD patterns of MFI type zeolites (A) and MWW type zeolites (B).

Raman spectra were collected to further understand the structure of  $\text{ReO}_x$  species on the zeolite supports. Prior to the  $\text{ReO}_x$  loading, MFI-type zeolites (MFI-40 and PMFI) exhibit a prominent peak at  $380 \text{ cm}^{-1}$ , as shown in Fig. 4(A), which can be assigned to the  $\delta_s$  (Si—O—Si) bending motion of the five membered-ring (5-MR) pore structure in MFI zeolite [56]. The other band at  $\sim 820 \text{ cm}^{-1}$  is due to the  $\nu_{\text{as}}$  (Si—O—Si) asymmetric stretching vibration, typical of all crystalline tetrahedral silica polymorphs [57]. After  $\text{ReO}_x$  loading, Re/MFI-15, Re/MFI-40, and Re/PMFI samples show the typical Raman peaks of MFI zeolite. In addition, two new peaks located at  $974$  and  $336 \text{ cm}^{-1}$ , corresponding to the  $\nu_s$  (O=Re=O) symmetric

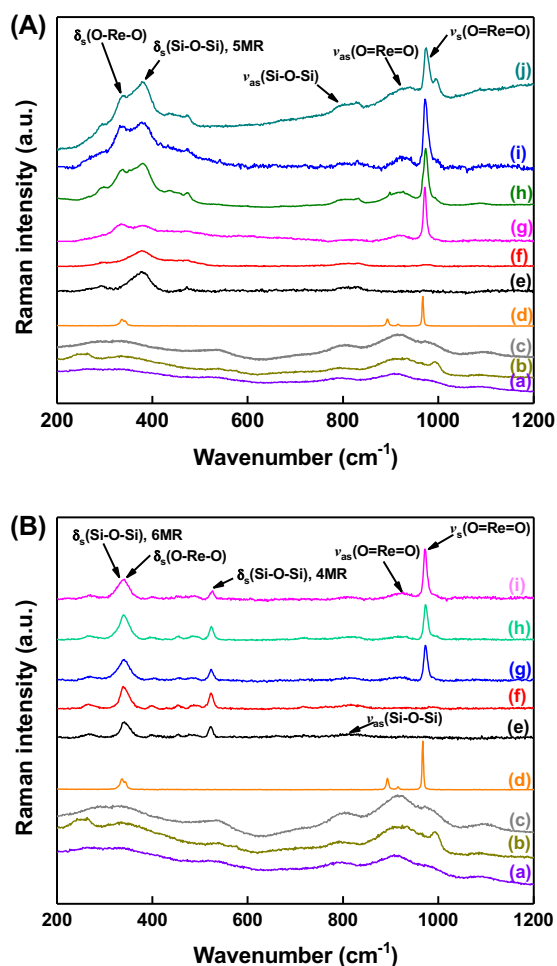


**Fig. 4.** Raman spectra of MFI type zeolites (A):  $\text{ReO}_2$  (a),  $\text{ReO}_3$  (b),  $\text{Re/SiO}_2$  (c),  $\text{NH}_4\text{ReO}_4$  (d), MFI-40 (e), PMFI (f), Re/MFI-15 (g), Re/MFI-40 (h), Re/PMFI (i), Re/MFI-10/5 (j), and MWW type zeolites (B):  $\text{ReO}_2$  (a),  $\text{ReO}_3$  (b),  $\text{Re/SiO}_2$  (c),  $\text{NH}_4\text{ReO}_4$  (d), MWW-20 (e), PMWW (f), Re/MWW-20 (g), Re/MWW-30 (h) and Re/PMWW (i).

stretching vibration and  $\delta_s$  (O—Re—O) bending vibration, respectively, were observed [47]. It is worth noting that the origin of the broad and weak band centered at  $922 \text{ cm}^{-1}$  remains elusive, as it has been reported to be due to the asymmetric stretching mode of terminal O=Re=O bonds [33,46,47], as well as the stretching mode of the bridging Re—O—Si bonds formed by breaking the framework Si—O—Si(or Al) bonds [58–60]. In addition, this weak  $922 \text{ cm}^{-1}$  band shows no notable changes across different samples. These vibration bands are different from those observed in  $\text{ReO}_2$ ,

ReO<sub>3</sub> and NH<sub>4</sub>ReO<sub>4</sub> compounds, but resemble the corresponding bands of aqueous ReO<sub>4</sub><sup>-</sup> anions with tetrahedral symmetry [47,61]. These results indicate that ReO<sub>x</sub> species had the isolated tetrahedral ReO<sub>4</sub><sup>-</sup> structure grafting at the acid sites in zeolite due to the hydration effect by adsorbed moisture. The thermal treatment that removes moisture in the samples can shift the Raman bands to higher frequencies, leading to a distorted tetrahedral structure, as have observed for ReO<sub>x</sub> species on metal oxide [11,38,62–67] and zeolite [46,47] supports. In addition, a small shoulder nearby 998 cm<sup>-1</sup> was observed in Re/MFI-40, Re/PMFI and Re/MFI-10/5 samples. This could be due to the ReO<sub>x</sub> species attached onto the silanol group or extra-framework Al in zeolite. Fig. 4(B) shows the MWW-type zeolites have intense Raman peaks at 338 cm<sup>-1</sup> and 525 cm<sup>-1</sup> that can be assigned to the δ<sub>s</sub> (Si–O–Si) bending motion of the 6-MR and 4-MR pore structures, respectively, in the MWW framework [68]. Similar to MFI zeolite framework in Fig. 4 (A), other peaks related to ν<sub>s</sub> (Si–O–Si) symmetric and ν<sub>as</sub> (Si–O–Si) asymmetric stretching vibrations, characteristics of crystalline tetrahedral silica polymorphs, are also observed in Fig. 4(B). The loading of ReO<sub>x</sub> in MWW-type zeolites generates two peaks at 974 and 927 cm<sup>-1</sup>, corresponding to the ν<sub>s</sub> (Re=O) symmetric and ν<sub>as</sub> (Re=O) asymmetric stretching vibrations of ReO<sub>x</sub> species, respectively. The δ<sub>s</sub> (O–Re–O) bending vibration overlaps with the δ<sub>s</sub> (Si–O–Si) bending motion of 6 MR at 338 cm<sup>-1</sup>, so it cannot be identified separately. The Raman spectra of Re/MWW-20, Re/MWW-30 and Re/PMWW indicate that the loaded ReO<sub>x</sub> species had the isolated ReO<sub>x</sub> species grafted on the acid sites, similar to that in MFI-type ReO<sub>x</sub>/zeolite samples. A small fraction of ReO<sub>x</sub> species might be associated with the silanol group or extra-framework Al in Re/MWW-30 and Re/PMWW zeolites, as hinted by the small shoulder peak at ~997 cm<sup>-1</sup> in Fig. 4(B).

XAS was carried out to reveal the oxidation states and coordination structures of ReO<sub>x</sub> species supported on zeolites, as shown in Fig. 5. The comparison between the Re L<sub>I</sub> edge and Re L<sub>III</sub> edge X-ray absorption spectra of references (Re foil, ReO<sub>2</sub>, ReO<sub>3</sub> and NH<sub>4</sub>ReO<sub>4</sub>) and zeolite samples in Fig. 5 suggests that all the ReO<sub>x</sub>/zeolite samples have the same oxidation state as NH<sub>4</sub>ReO<sub>4</sub> (+7), regardless of zeolite structure, acidity and mesoporosity. In Fig. 6, the Fourier-transformed k<sup>3</sup>-weighted χ(k) function (where k is wave number) shows that all the studied ReO<sub>x</sub>/zeolite samples only exhibit one pronounced peak at ~1.3 Å (phase uncorrected distance), which is assigned to the first-shell Re–O scattering. The absence of metallic Re–Re scattering confirms that no Re clusters are formed on the zeolite supports. The coordination number

(CN), interatomic distance (R), Debye-Waller factor (σ<sup>2</sup>) and inner potential correction (ΔE) of the EXAFS analysis are summarized in Table 3. The coordination number of ~4 in all samples suggests that the tetrahedrally coordinated ReO<sub>4</sub><sup>-</sup> structure was formed and the bond length of each Re–O bond is ~1.73–1.74 Å. This result is consistent with Raman data analyzed above.

### 3.3. Composition and Brønsted acid site concentration analyses

The bulk Si, Al and Re compositions of the ReO<sub>x</sub>/zeolite samples are summarized in Table 4. The MFI-15, MFI-40, MFI-10/5 and PMFI have Si/Al ratios of 16, 39, 31 and 75, respectively. These Si/Al ratios are very close to the Si and Al compositions branded by the commercial zeolites (MFI-15 and MFI-40) and used in the zeolite synthesis recipes (MFI-10/5 and PMFI). The MWW-20, MWW-30 and PMWW have Si/Al ratios of 24, 28 and 34, respectively, similar to those used in the synthesis. The Re concentrations in the studied zeolites varied in the range of 200–260 μmol g<sup>-1</sup>, which are lower than the Re loading amount (5 wt%, equivalent to 300 μmol g<sup>-1</sup>) in the ReO<sub>x</sub>/zeolite sample preparation. The loss of ReO<sub>x</sub> species could occur during the calcination step in the synthesis procedure, because ReO<sub>x</sub> sublimates at a temperature of ~500 K [47,69]. It should be noted that the ReO<sub>x</sub> quantity remained in zeolite supports after the entire synthesis procedure seems to be independent of zeolite topology and acidity.

The concentration of Brønsted acid sites in each zeolite was determined by the DME titration method. With increasing Si/Al ratio, the value of N<sub>tot,H</sub><sup>+</sup> decreases. The spatial distribution of Brønsted acid sites was determined by reaction rate loss in methanol dehydration with cumulative DTBP addition [37,51,52]. It is reported that DTBP has limited accessibility to micropores in MFI and MWW zeolites [70,71]. Therefore, DTBP dominantly poisons the Brønsted acid sites located on the external surface and mesopores. It is worth noting that MWW-type zeolites show much higher DTBP uptake than the MFI-type zeolites, due to the presence of 12-MR micropores (~0.76 nm in diameter), which has been reported to be partially accessible for DTBP [72–74]. Table 4 shows that the percentage of external Brønsted acid sites (f<sub>ext,H</sub><sup>+</sup>) increases with increasing mesoporosity in zeolites. In general, 2D zeolites have higher concentration of external Brønsted acid sites (N<sub>ext,H</sub><sup>+</sup>) than the 3D microporous analogues. The loading of ReO<sub>x</sub> species into zeolites led to a decrease of N<sub>tot,H</sub><sup>+</sup> in ReO<sub>x</sub>/zeolite samples, because ReO<sub>x</sub> species can anchor onto the Brønsted acid sites by replacing the protons [46,47].

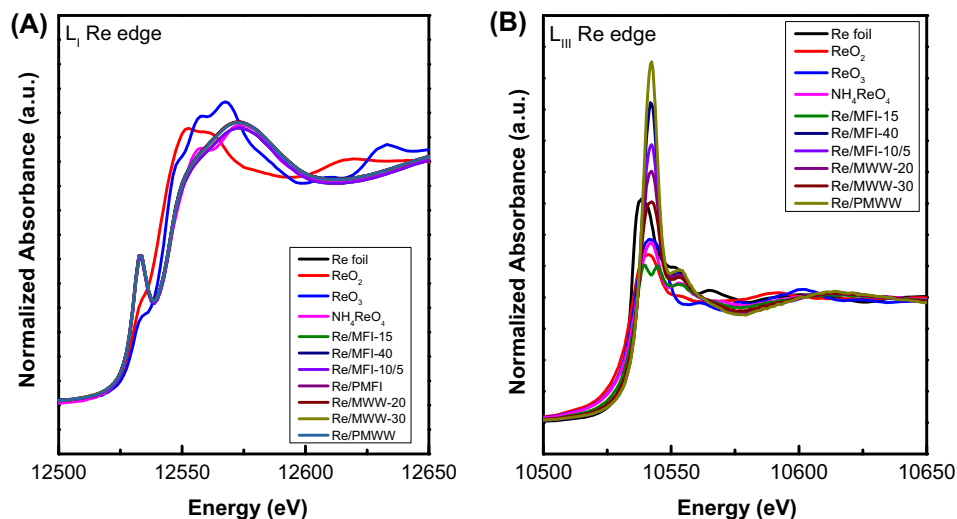


Fig. 5. Re L<sub>I</sub> edge (A) and Re L<sub>III</sub> edge (B) X-ray absorption spectra of Re references (Re foil, ReO<sub>2</sub>, ReO<sub>3</sub> and NH<sub>4</sub>ReO<sub>4</sub>), and ReO<sub>x</sub>/zeolite samples.

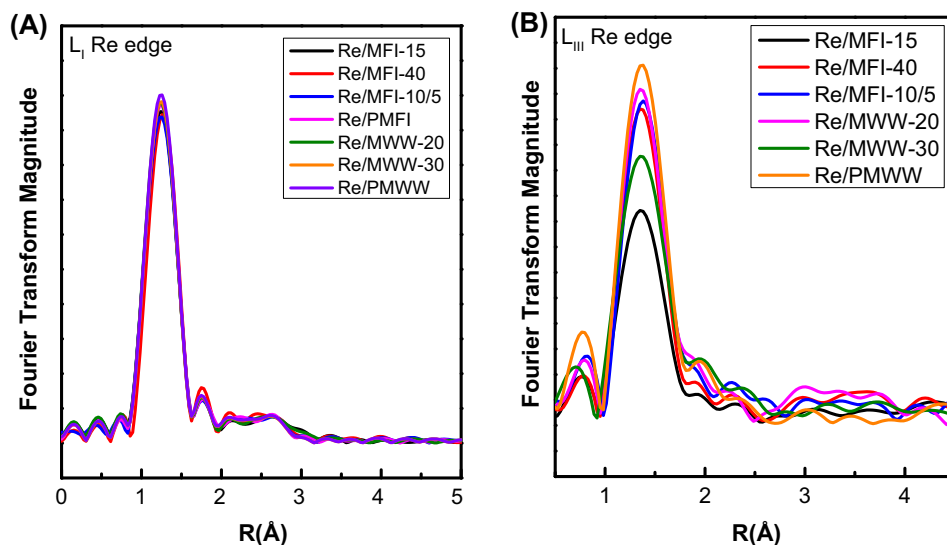


Fig. 6. Fourier transformed (FT)  $k^3$ -weighted  $\chi(k)$ -function of the EXAFS spectra based on Re  $L_1$  edge (A) and Re  $L_{III}$  edge (B) for  $ReO_x$ /zeolite samples.

Table 3

EXAFS fit parameters for  $ReO_x$  loaded zeolite samples with Re  $L_{III}$  edge ( $k^2$ :  $\Delta k = 3 - 12 \text{ \AA}^{-1}$  and  $\Delta r = 1 - 3 \text{ \AA}$ ).

Re/Zeolite	$N_{Re=O}$	$R_{Re=O}$ ( $\text{\AA}$ )	$\sigma^2$ ( $\text{\AA}^2$ )	$\Delta E$ (eV)
Re/MFI-15	$3.8 \pm 0.5$	$1.74 \pm 0.01$	0.002	8.4
Re/MFI-40	$3.9 \pm 0.5$	$1.73 \pm 0.01$	0.002	8.0
Re/MFI-10/5	$4.0 \pm 0.6$	$1.73 \pm 0.01$	0.003	8.2
Re/MWW-20	$3.8 \pm 0.5$	$1.73 \pm 0.01$	0.002	8.3
Re/MWW-30	$3.7 \pm 0.5$	$1.73 \pm 0.01$	0.002	8.2
Re/PMWW	$4.3 \pm 0.4$	$1.73 \pm 0.01$	0.003	7.3

The percentage of external acid sites in the  $ReO_x$ /zeolite samples was determined using the DME/DTBP titration method, in which samples were pretreated by DTBP vapor carried by He flow, resulting in the deactivation of external acid sites. The subsequent DME titration can exclusively determine the amount of internal acid sites ( $N_{int,H}^+$ ), and the amount of external acid sites ( $N_{ext,H}^+$ ), in turn, is calculated by abstracting the  $N_{int,H}^+$  from the total amount of acid sites in  $ReO_x$ /zeolite samples obtained by the regular DME titration. As shown in Table 4, Re/MFI-15 and Re/MFI-40 samples have negligible percentages of external acid sites due to limited external surfaces. The Re/MFI-10/5 and Re/PMFI have 5% and 14% of external acid sites, which are lower than those for the samples prior to  $ReO_x$  loading. Similarly, Re/MWW-20 and Re/MWW-30 have lower percentages of external acid sites than MWW-20 and

MWW-30 samples. Re/PMWW has comparable percentage of external acid sites to PMWW zeolite. The results on acid site concentrations and locations indicate that  $ReO_x$  species do not have uniform distribution throughout all the studied zeolite supports. Instead, they are affected by zeolite type and mesoporosity.

#### 3.4. Anchoring nature and spatial distribution of $ReO_x$ species on zeolite supports

$ReO_x$ /zeolite catalysts have been previously prepared by loading  $ReO_x$  species onto zeolite frameworks of MFI, BEA, FAU and MOR, in which Si/Al ratios were varied from 10 to 110 and Re concentrations were typically controlled between 0.4 wt% and 10 wt% [41,42,46,47,75]. The study on  $ReO_x$  structures in zeolite supports, however, has been mainly focused on  $ReO_x$ /MFI catalysts with Si/Al ratio <20 [46,47]. It is found that, under ambient conditions, the  $ReO_x$  species behave like  $ReO_4^-$  anions in aqueous solution due to the hydration by adsorbed moisture in zeolite supports. Under dehydration treatment in flowing dry air at high temperature,  $ReO_x$  species interacts with Brønsted acid sites of zeolites to form  $O_2Re(\mu-O_2)ReO_2^+$  dimer or  $Si-O_2ReO_3-Al$  monomer [46,47]. In either case, the replacement of protons in  $Si-OH^+-Al$  sites by  $ReO_x$  follows  $H^+/Re = 1.1 \pm 0.1$ . In the present study, besides MFI zeolite with Si/Al ratio of 15, MFI and MWW zeolites with higher Si/Al ratios and micro-/mesoporosity were employed. As discussed above, 2D

Table 4

Composition and acidity of zeolite samples before and after loading of  $ReO_x$ .

Zeolite	Si/Al <sup>a</sup>	$N_{tot,H}^+$ ( $\mu\text{mol g}^{-1}$ )	Before $ReO_x$ loading		After $ReO_x$ loading			$N_{tot,H}^+/Re^d$
			$N_{tot,H}^+$ ( $\mu\text{mol g}^{-1}$ )	$f_{ext,H}^+$ (%)	$N_{tot,H}^+$ ( $\mu\text{mol g}^{-1}$ )	$f_{ext,H}^+$ (%)	$N_{tot,Re}^+$ ( $\mu\text{mol g}^{-1}$ )	
MFI-15	16	882	846	–	579	–	258	3.28
MFI-40	39	375	378	–	295	–	252	1.50
MFI-10/5	31	469	387	10	278	5	204	1.90
PMFI	75	197	185	36	89	14	260	0.71
MWW-20	24	600	623	20	372	13	232	2.69
MWW-30	28	517	401	24	330	21	245	1.64
PMWW	34	429	327	67	248	67	238	1.37

<sup>a</sup> Measured by ICP-OES.

<sup>b</sup> Total concentration of Brønsted acid sites in zeolites determined by DME titration.

<sup>c</sup> Fraction of external acid sites in zeolites determined by methanol dehydration in presence of DTBP.

<sup>d</sup> Calculated by  $N_{tot,H}^+/Re = N_{tot,H}^+ (\text{before } ReO_x \text{ loading})/N_{tot,Re}^+$

lamellar PMFI and PMWW zeolites have high percentages of external Si-OH<sup>+</sup>-Al acid sites. We, therefore, would like to explore how the acidity and porosity impact the anchoring structure of ReO<sub>x</sub> species and their spatial distribution on these zeolite supports.

### 3.4.1. Effects of zeolite acidity and mesoporosity on anchoring structure of ReO<sub>x</sub> species

As summarized in Table 4, the total concentrations of Brønsted acid sites (N<sub>tot,H</sub><sup>+</sup>) in zeolite and ReO<sub>x</sub>/zeolite samples have been quantified by organic base titrations. The difference between these two sets of N<sub>tot,H</sub><sup>+</sup> data indicates the loss of Brønsted acid sites (ΔN<sub>tot,H</sub><sup>+</sup>) due to ReO<sub>x</sub> addition. Since the percentages of external Brønsted acid sites in zeolites before and after ReO<sub>x</sub> loading are known, the changes in concentrations of internal (ΔN<sub>int,H</sub><sup>+</sup>) and external (ΔN<sub>ext,H</sub><sup>+</sup>) Brønsted acid sites in each zeolite can be calculated using the following equations:

$$N_{\text{int,H}}^+ = N_{\text{tot,H}}^+ \times (1 - f_{\text{ext,H}}^+)$$

$$\Delta N_{\text{int,H}}^+ = N_{\text{int,H}}^+(\text{before ReO}_x \text{ loading}) - N_{\text{int,H}}^+(\text{after ReO}_x \text{ loading})$$

$$\Delta N_{\text{ext,H}}^+ = \Delta N_{\text{tot,H}}^+ - \Delta N_{\text{int,H}}^+$$

Table 5 summarizes the values of ΔN<sub>tot,H</sub><sup>+</sup>, ΔN<sub>int,H</sub><sup>+</sup> and ΔN<sub>ext,H</sub><sup>+</sup> for each zeolite upon ReO<sub>x</sub> loading. The ratio of Re concentration to the concentration variation of Brønsted acid sites (i.e., Re/ΔN<sub>tot,H</sub><sup>+</sup>) is thus calculated. For MFI-15 and MWW-20 zeolites, the Re/ΔN<sub>tot,H</sub><sup>+</sup> ratios are 0.97 and 0.92, respectively. This means that the replacement of protons in Si-OH<sup>+</sup>-Al sites by ReO<sub>x</sub> follows H<sup>+</sup>/Re = 1.1 ± 0.1 stoichiometry, consistent with previous reports [46,47]. The ReO<sub>x</sub> species predominately reside on internal Brønsted acid sites in these two zeolites.

The increase in Si/Al ratio (or decrease in acidity) in zeolite leads to an increase in the Re/ΔN<sub>tot,H</sub><sup>+</sup> ratio. As shown in Table 5, Re/MFI-40 and Re/MWW-30 have the Re/ΔN<sub>tot,H</sub><sup>+</sup> ratios of 3.03 and 3.48, respectively. In other words, the H<sup>+</sup>/Re ratios are 0.33 and 0.29, accordingly, in Re/MFI-40 and Re/MWW-30 samples. The last entry in Table 4 indicates that the concentration of Brønsted acid sites in all the zeolite samples, except for PMFI, is higher than that of the ReO<sub>x</sub> loaded. The lower H<sup>+</sup>/Re ratio is not caused by the shortage of free Si-OH<sup>+</sup>-Al sites. The increase in zeolite mesoporosity improved the anchoring of ReO<sub>x</sub> species onto Si-OH<sup>+</sup>-Al sites, reflected by the lower Re/ΔN<sub>tot,H</sub><sup>+</sup> ratios, 2.72 and 3.02, respectively, for Re/PMFI and Re/PMWW samples compared to Re/MFI-40 and Re/MWW-30 samples. MFI-10/5 has lower Si/Al ratio and higher mesoporosity than MFI-40, and the corresponding Re/ΔN<sub>tot,H</sub><sup>+</sup> value is 1.88. Clearly, the acidity impacts significantly on the replacement ratio between protons in Si-OH<sup>+</sup>-Al acid sites

and ReO<sub>x</sub> species, while mesoporosity gently improves the anchoring of ReO<sub>x</sub> onto Si-OH<sup>+</sup>-Al sites in ReO<sub>x</sub>/zeolite samples. The higher Re/ΔN<sub>tot,H</sub><sup>+</sup> ratio than one-to-one stoichiometry in ReO<sub>x</sub>/zeolite samples suggests that a large concentration of ReO<sub>x</sub> species resided on places other than Brønsted acid sites in zeolites with high Si/Al ratios.

As an analogue to ReO<sub>x</sub>, MoO<sub>x</sub> supported on zeolite has been studied more thoroughly in literature. A report by Gao, et al. [15] has revealed that MoO<sub>x</sub> species can react with the protons of silanol groups (Si-OH) and extra-framework Al-OH groups in the MFI zeolite when the Si/Al ratio is high. The study by Iglesia's group also indicated that ReO<sub>x</sub> species can interact with the Si-OH groups to form O<sub>3</sub>Si-ReO<sub>3</sub> structure in zeolite support, although the Si/Al ratio of zeolite in their study was as low as 13.4 [46,47]. We, therefore, hypothesize that a significant portion of ReO<sub>x</sub> species is associated with silanol groups in zeolite supports that have high Si/Al ratio and/or mesoporosity.

In order to verify our hypothesis, *in-situ* DRIFTS spectra were collected on the zeolites before and after ReO<sub>x</sub> loading, respectively. Fig. 7 shows all the DRIFTS spectra of studied samples across the frequency of the OH-stretching mode (ν(OH)). The vibrational modes at 3760–3695 cm<sup>-1</sup> are associated with ν(OH) of terminal silanol groups, while peaks at 3695–3535 cm<sup>-1</sup> are related to the acidity (Lewis and Brønsted acid sites) in zeolites [76–78]. In particular, the peaks centered at 3733 cm<sup>-1</sup>, 3650 cm<sup>-1</sup> and 3595 cm<sup>-1</sup> can be assigned to the silanol groups (Si-OH), extra-framework (Al-OH) and Brønsted acid sites (Si-OH<sup>+</sup>-Al), respectively [78]. Compared to MFI-40 and MWW-30, MFI-15 and MWW-20 have a much larger Brønsted acid site peak, consistent with their higher amount of acid sites determined by the DME titration. The 2D lamellar MFI-10/5, PMFI and PMWW have much larger Si-OH peaks than the corresponding 3D MFI and MWW zeolites. The incorporation of ReO<sub>x</sub> species apparently led to the decrease in DRIFTS peak intensity at positions of Si-OH<sup>+</sup>-Al and terminal Si-OH groups in each zeolite, which confirms our hypothesis that both Brønsted acid sites and silanol groups can anchor the ReO<sub>x</sub> species in zeolites with low acidity and/or mesoporosity. Since the IR band associated with the extra-framework Al-OH sites is nearly negligible, particularly for MFI-40 and MWW-30, the chance of Al-OH acting as the anchoring site seems to be low, and thus, we propose that the silanol groups are the main alternative to Si-OH<sup>+</sup>-Al sites when anchoring ReO<sub>x</sub> species.

To further understand the inter-dependence of the loaded ReO<sub>x</sub> species and the associated Brønsted acid sites and silanol groups, the variation in peak areas of the bands centered at 3733 cm<sup>-1</sup> (I<sub>Si-OH</sub><sup>+</sup>) and 3595 cm<sup>-1</sup> (I<sub>H</sub><sup>+</sup>) were calculated for all the samples. The quantitative analysis for catalyst properties from DRIFTS spectra is challenging due to a range of extinction coefficients reported in previous studies [79–81]. Here, we follow the procedure

**Table 5**  
Zeolite acidity change due to ReO<sub>x</sub> loading and spatial distribution of ReO<sub>x</sub> species in Re/zeolite samples.

Re/Zeolite	ΔN <sub>tot,H</sub> <sup>+</sup> <sup>a</sup> (μmol g <sup>-1</sup> )	ΔN <sub>int,H</sub> <sup>+</sup> <sup>b</sup> (μmol g <sup>-1</sup> )	ΔN <sub>ext,H</sub> <sup>+</sup> <sup>c</sup> (μmol g <sup>-1</sup> )	Re/ΔN <sub>tot,H</sub> <sup>+</sup> <sup>d</sup>	Re <sub>int,H</sub> <sup>+</sup> <sup>e</sup> (%)	Re <sub>ext,H</sub> <sup>+</sup> <sup>f</sup> (%)	Re <sub>Si-OH</sub> <sup>g</sup> (%)
Re/MFI-15	267	267	–	0.97	100	–	0
Re/MFI-40	83	83	–	3.03	30	–	70
Re/MFI-10/5	109	85	24	1.88	37	13	52
Re/PMFI	96	42	53	2.72	15	23	66
Re/MWW-20	251	174	77	0.92	67	33	0
Re/MWW-30	71	44	27	3.48	16	10	74
Re/PMWW	79	26	53	3.02	10	20	70

<sup>a</sup> Calculated by ΔN<sub>tot,H</sub><sup>+</sup> = N<sub>tot,H</sub><sup>+</sup> (before ReO<sub>x</sub> loading) – N<sub>tot,H</sub><sup>+</sup> (after ReO<sub>x</sub> loading).

<sup>b</sup> Calculated by ΔN<sub>int,H</sub><sup>+</sup> = N<sub>tot,H</sub><sup>+</sup> × (1 – f<sub>ext,H</sub><sup>+</sup>) (before ReO<sub>x</sub> loading) – N<sub>tot,H</sub><sup>+</sup> × (1 – f<sub>ext,H</sub><sup>+</sup>) (after ReO<sub>x</sub> loading).

<sup>c</sup> Calculated by ΔN<sub>ext,H</sub><sup>+</sup> = ΔN<sub>tot,H</sub><sup>+</sup> – ΔN<sub>int,H</sub><sup>+</sup>.

<sup>d</sup> Evaluated by Re/ΔN<sub>tot,H</sub><sup>+</sup> = N<sub>tot,Re</sub>/ΔN<sub>tot,H</sub><sup>+</sup>.

<sup>e</sup> Evaluated by Re<sub>int,H</sub><sup>+</sup> = ΔN<sub>int,H</sub><sup>+</sup>/N<sub>tot,Re</sub> × 100.

<sup>f</sup> Evaluated by Re<sub>ext,H</sub><sup>+</sup> = ΔN<sub>ext,H</sub><sup>+</sup>/N<sub>tot,Re</sub> × 100.

<sup>g</sup> Evaluated by Re<sub>Si-OH</sub> = 100 – Re<sub>int,H</sub><sup>+</sup> – Re<sub>ext,H</sub><sup>+</sup>.

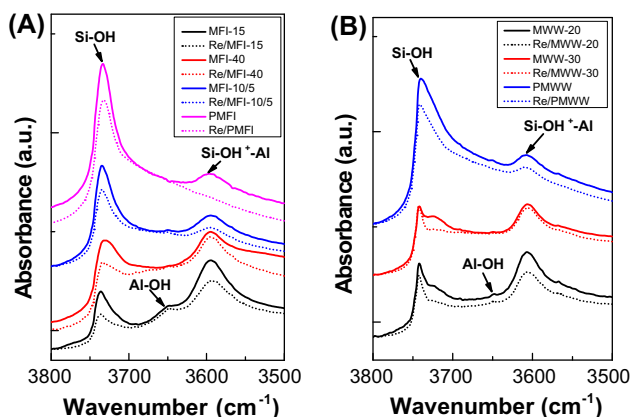


**Fig. 7.** DRIFTS spectra of MFI-type (A) and MWW-type (B) zeolites before and after  $\text{ReO}_x$  loading, respectively. The spectra were normalized to the overtone and combination vibrations found between 1750 and 2100  $\text{cm}^{-1}$  in each spectrum that was used as an internal standard.

reported by Bräuer et al. [76,77] to carry out the quantitative analysis without using the extinction coefficient. The DRIFTS spectra in the absorbance mode (Fig. 7) were normalized to the overtone and combination  $\text{Si-O-Si}$  vibrations found between 1750 and 2100  $\text{cm}^{-1}$  ( $I_{1750-2100}$ ) in each spectrum that was used as an internal standard. Hence, all integrated peak areas (or intensities) were calculated by the equations:  $I_{\text{H}^+} = I_{3595}/I_{1750-2100}$  and  $I_{\text{Si-OH}} = I_{3733}/I_{1750-2100}$ .

Table 6 summarizes the values of  $I_{\text{H}^+}$  and  $I_{\text{Si-OH}}$  in zeolite, as well as their changes ( $\Delta I_{\text{H}^+}$  and  $\Delta I_{\text{Si-OH}}$ ) after  $\text{ReO}_x$  loading. The increase in Si/Al ratio in zeolites leads to a decrease in  $I_{\text{H}^+}$  and slight change in  $I_{\text{Si-OH}}$ . The increase in mesoporosity significantly improves  $I_{\text{Si-OH}}$ , compared to 3D zeolites. The same trends are found in Re/zeolite samples. The ratio of  $\Delta I_{\text{Si-OH}}$  to  $\Delta I_{\text{H}^+}$  ( $\Delta I_{\text{Si-OH}}/\Delta I_{\text{H}^+}$ ) was calculated and shows an increase with increasing Si/Al ratio and mesoporosity. In particular, micro-/mesoporous 2D lamellar PMFI and PMWW zeolites have very high  $\Delta I_{\text{Si-OH}}/\Delta I_{\text{H}^+}$  ratios compared to the microporous MFI and MWW zeolites. These results suggest that Si-OH groups in 2D zeolites should play a significant role as the anchoring sites for  $\text{ReO}_x$  species.

### 3.4.2. Effects of zeolite acidity and mesoporosity on spatial distribution of $\text{ReO}_x$ species

Combining the characterizations thus far, as well as the  $\text{H}^+/\text{Re} = 1.1 \pm 0.1$  replacement stoichiometry between  $\text{ReO}_x$  and Brønsted acid sites reported in literature [46,47], quantification on spatial distribution of Brønsted acid sites in zeolites from our previous work [16,72], and the Brønsted acid sites and Si-OH

groups in DRIFTS measurement, we can formulate an overall picture of spatial distribution of  $\text{ReO}_x$  in zeolite supports, as shown in Scheme 1. As listed in Table 5, the loss of internal and external acid sites in  $\text{ReO}_x/\text{zeolite}$  samples were evaluated. These values reflect the concentrations of  $\text{ReO}_x$  species on internal and external Si-OH<sup>+</sup>-Al sites if we assume the  $\text{H}^+/\text{Re} = 1.1$  stoichiometry. Since the bulk  $\text{ReO}_x$  concentration in each sample is known (as shown by the second last entry in Table 4), the concentration of  $\text{ReO}_x$  species on Si-OH groups can be calculated by  $N_{\text{Si-OH,Re}} = N_{\text{tot,Re}} - (\Delta N_{\text{int,H}} + \Delta N_{\text{ext,H}})/1.1$ . The percentages of  $\text{ReO}_x$  species in each location, i.e., internal ( $\text{Re}_{\text{int,H}}^+$ ) and external ( $\text{Re}_{\text{ext,H}}^+$ ) Si-OH<sup>+</sup>-Al sites as well as Si-OH groups ( $\text{Re}_{\text{Si-OH}}$ ) can be determined, and the results are shown in Table 5.

In microporous zeolite supports with low Si/Al ratios (Re/MFI-15 and Re/MWW-20), nearly all  $\text{ReO}_x$  resided on the internal Brønsted acid sites in zeolite micropores. The increase in Si/Al ratio zeolites, for example, Re/MFI-40 and Re/MWW-30 samples, led to migration of a significant portions ( $\text{Re}_{\text{Si-OH}} = 70\%$  and  $74\%$ , respectively) of  $\text{ReO}_x$  onto Si-OH groups. In 2D lamellar Re/PMFI and Re/PMWW samples, the  $\text{ReO}_x$  species distributed on internal and external Si-OH<sup>+</sup>-Al sites as well as on Si-OH groups. Re/MFI-10/5 has  $\text{Re}_{\text{Si-OH}}$  of 52%, lower than Re/MFI-40, although it has higher mesoporosity. Despite the fact that the presence of mesoporosity is helpful for migration of  $\text{ReO}_x$  species onto Si-OH<sup>+</sup>-Al sites ( $\text{Re}_{\text{Si-OH}} = 66\%$  and  $70\%$ , respectively, in Re/PMFI and Re/PMWW), the acidity seems to dominantly impact the distribution of  $\text{ReO}_x$  species on Si-OH groups.

To verify our assumption for replacement stoichiometry between  $\text{ReO}_x$  and Si-OH<sup>+</sup>-Al sites in zeolite supports with high Si/Al ratio and mesoporosity, we plotted the peak area of  $I_{\text{H}^+}$  from DRIFTS spectra versus Si-OH<sup>+</sup>-Al acid site concentration ( $N_{\text{tot,H}}^+$ ) determined by organic base titration for all the zeolite and  $\text{ReO}_x/\text{zeolite}$  samples. As shown in Fig. 8(A),  $I_{\text{H}^+}$  increases linearly with the concentration of Si-OH<sup>+</sup>-Al sites in both MFI and MWW-type samples, albeit with different slopes. This indicates that the 3595  $\text{cm}^{-1}$  ( $I_{\text{H}^+}$ ) band in DRIFTS can be used as a tool to quantitatively evaluate the concentration of Si-OH<sup>+</sup>-Al sites in zeolites. The different slopes likely represent differences in the extinction coefficients of the acid sites in the two kinds of structures, as has been previously reported [81]. Since the linear correlation between  $I_{\text{H}^+}$  and Si-OH<sup>+</sup>-Al sites is valid for zeolite before and after  $\text{ReO}_x$  loading in Fig. 8(A), the linear correlation between  $\Delta I_{\text{H}^+}$  and  $\text{ReO}_x$  anchored on Brønsted acid sites is thus expected. This is consistent with the  $\text{H}^+/\text{Re} = 1.1 \pm 0.1$  replacement stoichiometry between  $\text{ReO}_x$  and Brønsted acid sites in MFI-15 and MWW-20 samples that were determined by the organic base titration experiment. Unfortunately, we could not directly quantify the concentration of  $\text{ReO}_x$  species on Brønsted acid sites in zeolites with high Si/Al ratio and/or mesoporosity. The presence of distorted tetrahedral coordina-

**Table 6**

Quantitative analysis of peak intensities of Brønsted acid site and terminal silanol group in DRIFTS spectra of zeolite and Re/zeolite samples, respectively.

Zeolites	Before $\text{ReO}_x$ loading		After $\text{ReO}_x$ loading		$\Delta I_{\text{H}^+}^c$	$\Delta I_{\text{Si-OH}}^d$	$\Delta I_{\text{Si-OH}}/\Delta I_{\text{H}^+}^e$
	$I_{\text{H}^+}^a$	$I_{\text{Si-OH}}^b$	$I_{\text{H}^+}^a$	$I_{\text{Si-OH}}^b$			
MFI-15	0.193	0.096	0.120	0.050	0.073	0.046	0.630
MFI-40	0.071	0.101	0.049	0.054	0.022	0.046	2.091
MFI-10/5	0.085	0.256	0.051	0.211	0.034	0.044	1.294
PMFI	0.0419	0.362	0.011	0.196	0.042	0.166	3.952
MWW-20	0.244	0.056	0.161	0.050	0.083	0.006	0.072
MWW-30	0.155	0.041	0.112	0.032	0.043	0.009	0.209
PMWW	0.0358	0.330	0.024	0.246	0.011	0.084	7.636

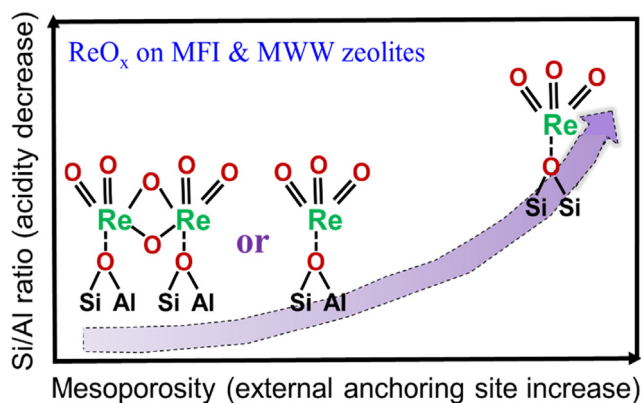
<sup>a</sup> Peak area of  $\nu(\text{Si-OH}^+-\text{Al})$  band centered at 3595  $\text{cm}^{-1}$ .

<sup>b</sup> Peak area of  $\nu(\text{Si-OH})$  band in the range of 3760–3695  $\text{cm}^{-1}$ .

<sup>c</sup> Reduction in peak area of  $\nu(\text{Si-OH}^+-\text{Al})$  in zeolite after  $\text{ReO}_x$  loading.

<sup>d</sup> Reduction in peak area of  $\nu(\text{Si-OH})$  in zeolite after  $\text{ReO}_x$  loading.

<sup>e</sup> Ratio of decrease in Si-OH group to decrease in Si-OH<sup>+</sup>-Al sites due to  $\text{ReO}_x$  loading in zeolite samples.



**Scheme 1.** Anchoring structures of ReO<sub>x</sub> species in MFI and MWW zeolites with various acidity and mesoporosity.

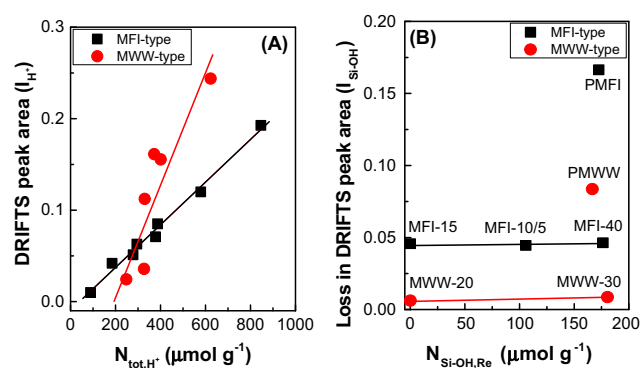


**Fig. 8.** (A) Peak area of (Si-(OH\*)-Al) acid sites in DRIFTS versus acid site concentration determined by DME titration in MFI-type and MWW-type zeolites, before and after ReO<sub>x</sub> loading. (B) Loss in peak area of (Si-OH) groups in DRIFTS upon ReO<sub>x</sub> loading versus ReO<sub>x</sub> on Si-OH groups from site balance analysis.

tion of Si-O<sub>7</sub>ReO<sub>3</sub>-Al monomer, determined from the Raman data, however, suggests the H<sup>+</sup>/Re = 1.1 ± 0.1 replacement stoichiometry is valid in these zeolite samples. Overall, it seems that the H<sup>+</sup>/Re = 1.1 ± 0.1 replacement stoichiometry between ReO<sub>x</sub> and Brønsted acid sites is applicable to all the studied samples, irrespective of the support acidity and mesoporosity.

To explore the correlation between  $N_{\text{Si-OH,Re}}$  and the loss in peak area of Si-OH group ( $I_{\text{Si-OH}}$ ) in DRIFTS spectra, we plotted the  $I_{\text{Si-OH}}$  versus  $N_{\text{Si-OH,Re}}$  for the studied samples, as shown in Fig. 8(B). First of all, the peak area of Si-OH groups in MFI-15 and MWW-20 was decreased upon ReO<sub>x</sub> loading. As noted in Section 3.4.1, this could be caused by the formation of O<sub>3</sub>Si-ReO<sub>3</sub> species on external surface Si-OH groups [46,47]. Secondly, the loss in peak area of Si-OH groups seems to increase slightly when only Si/Al ratio of zeolite (i.e., MFI-10/5, MFI-40 and MWW-30) is increased. However, we would nominally expect for a much higher loss in peak area of Si-OH groups on the basis of ReO<sub>x</sub> assigned onto the Si-OH group in these samples. This inconsistency might suggest that ReO<sub>x</sub> does not follow the one-to-one replacement ratio between Si-OH and ReO<sub>x</sub> species. The anchoring of ReO<sub>x</sub> species onto extra-framework acid sites (for example, Al-OH groups) in zeolite support could also contribute to this inconsistency. Thirdly, in 2D lamellar micro-/mesoporous PMFI and PMWW zeolites, a significant decrease in Si-OH peak area was observed upon inclusion of ReO<sub>x</sub> species into these zeolite supports. Lastly, the notable differences in the loss of Si-OH peak area between MFI and MWW-type zeolites might be due to the different Si-OH density in both materials. As reported in our previous work, the number of silanol

groups per unit cell of a single-unit-cell thick MWW nanosheet is 8 times lower than that of a single-unit-cell thick MFI nanosheets [52]. Overall, the quantitative correlation is not found between  $I_{\text{Si-OH}}$  and  $N_{\text{Si-OH,Re}}$  in all the studied zeolite samples, but the mesoporosity in 2D zeolites contributes to the formation of Si-OH groups, and the consequent anchoring sites for ReO<sub>x</sub> species.

### 3.5. Influence of anchoring structure of ReO<sub>x</sub> species on zeolite supports on DNMC reaction.

The difference in anchoring structure and spatial distribution of ReO<sub>x</sub> species on zeolite supports can lead to difference in catalytic performances. To study the implication of this effects, the DNMC reaction was studied on Re/MFI-15, Re/MFI-30 and Re/PMFI, as well as Re/MWW-20, Re/MWW-30 and Re/PMWW catalysts. For comparison, the same reaction was run on the ReO<sub>x</sub> supported on silica (Re/SiO<sub>2</sub>) catalyst. The Re/SiO<sub>2</sub> catalyst was prepared using the same procedure as that of ReO<sub>x</sub>/zeolite samples, except that zeolite was replaced by the fume silica. Fig. 9(A) shows the product formation rate, i.e., a combination of formation rates of C<sub>2</sub>, benzene and naphthalene, as a function of the type of ReO<sub>x</sub>/zeolite catalysts. It should be noted that all the catalysts contain similar loadings of Re (~5 wt%). The product formation rate increases with  $\text{Re}_{\text{int,H}^+}$  in MFI-type zeolites. The very low reaction rate of DNMC on Re/SiO<sub>2</sub> suggests that the sole presence of Re sites does not enable DNMC reaction effectively. It requires the Brønsted acid sites to work cooperatively to cyclize the C<sub>2</sub> species formed from methane activation on Re sites [5,13]. Fig. 9(B) shows the benzene, naphthalene and C<sub>2</sub> selectivity in DNMC over each catalyst. The benzene product only formed on the ReO<sub>x</sub>/zeolite catalyst, presumably on the samples with  $\text{Re}_{\text{int,H}^+}$  sites. Its selectivity increases with increasing  $\text{Re}_{\text{int,H}^+}$  sites. The naphthalene formed on external  $\text{Re}_{\text{ext,H}^+}$  and  $\text{Re}_{\text{Si-OH}}$  sites, as well as on internal  $\text{Re}_{\text{int,H}^+}$  sites. A balance between these two classes of sites minimizes its selectivity. For example, Re/SiO<sub>2</sub> has higher naphthalene selectivity than Re/PMFI, but it does not have  $\text{Re}_{\text{int,H}^+}$  sites. The naphthalene selectivity in these three zeolite-based catalysts follows the sequence of Re/MFI-15 > Re/MFI-40 > Re/PMFI. Apparently, the higher number of  $\text{Re}_{\text{int,H}^+}$  sites enabled more cyclization reactions in the zeolite micropores, in which heavier naphthalene product forms [16]. The C<sub>2</sub> product selectivity increases with increasing  $\text{Re}_{\text{ext,H}^+}$  and/or  $\text{Re}_{\text{Si-OH}}$  quantity. The dependence of reaction rate and product selectivity on the location of ReO<sub>x</sub> in MWW zeolites, i.e., Re/MWW-20, Re/MWW-30 and Re/PMWW, is similar to those observed in ReO<sub>x</sub>/MFI catalysts, as shown in Fig. 9(C-D). The full sets of product formation rates and selectivities versus time-on-stream in DNMC over all the studied catalysts are shown in Figs. S1 and S2 of the supporting information.

The quantitative correlations between the catalytic performance in DNMC and catalyst properties were further analyzed and are shown in Fig. 10. Firstly, the product formation rate is linearly proportional to the ratio of internal Brønsted acid site concentration to ReO<sub>x</sub> active site concentration, i.e.,  $N_{\text{int,H}^+}/N_{\text{tot,Re}}$ , in either MFI- or MWW-type zeolite framework, as indicated in Fig. 10(A). Since  $N_{\text{tot,Re}}$  is similar across all the ReO<sub>x</sub>/MFI or ReO<sub>x</sub>/WW samples, we could interpret that  $N_{\text{int,H}^+}$  highly influences the reaction rate. We tried to plot the product formation rate versus  $N_{\text{int,H}^+}$  solely, but the plot is much less linear compared to that in Fig. 10(A). This indicates that Re sites also contributes to product formation in the DNMC reaction. Overall, both metal and internal Brønsted acid site should work cooperatively to facilitate the DNMC reaction. Fig. 10(B) shows that benzene product selectivity increases linearly with an increase in the percentage of internal Re sites, i.e.,  $\text{Re}_{\text{int,H}^+}$  sites anchored onto internal Brønsted acid sites in zeolite micropores. The further increase in  $\text{Re}_{\text{int,H}^+}$  sites, however, leads to a plateau in Fig. 10(B). The acidity and structure

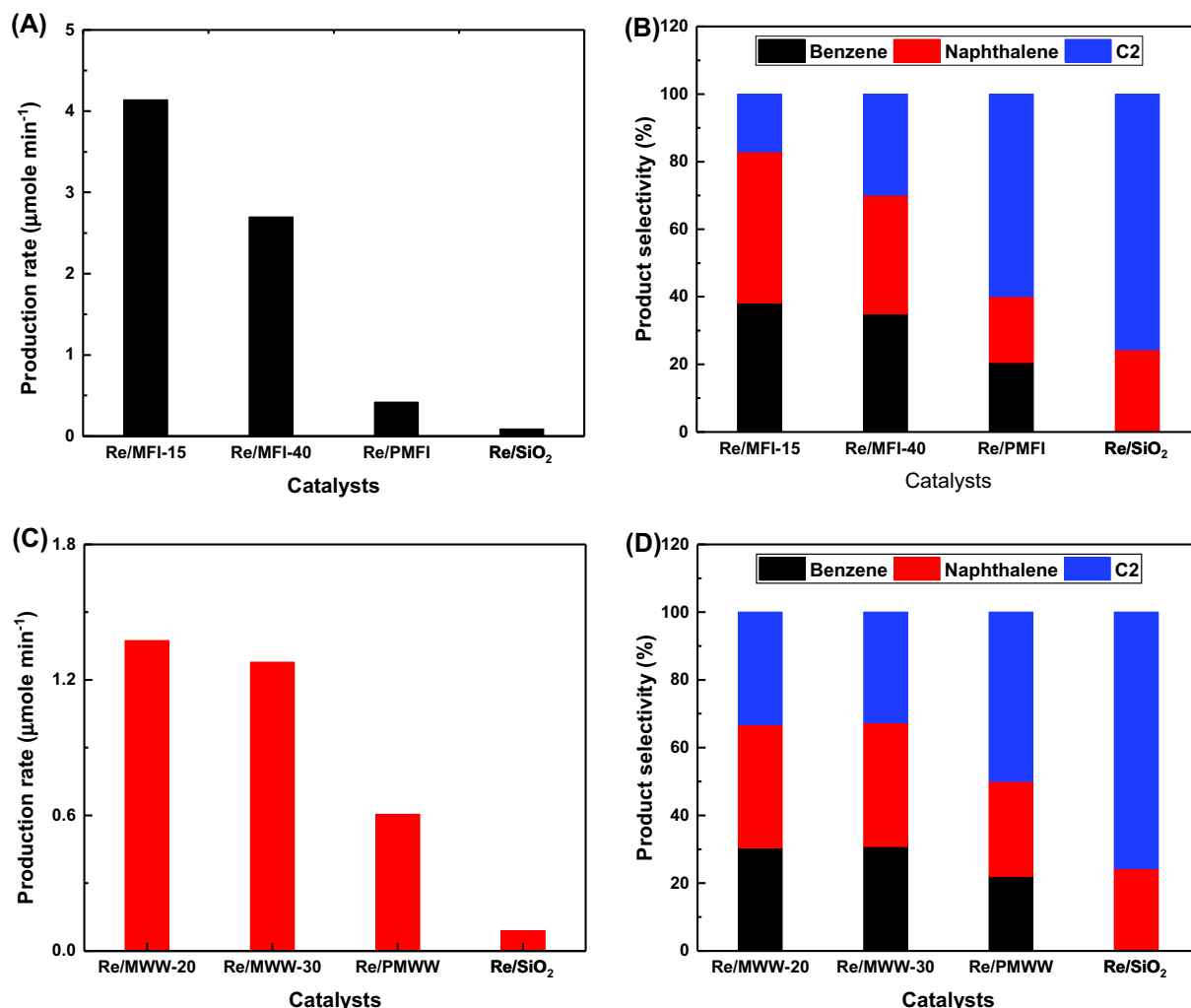


Fig. 9. Product formation rate (A) and selectivity (B) in DNMC over ReO<sub>x</sub>/MFI zeolite catalysts, and product formation rate (C) and selectivity (D) over ReO<sub>x</sub>/MWW zeolite catalysts. (Both product formation rate and selectivity are shown on the C-atom basis at the reaction time of 4.35 h).

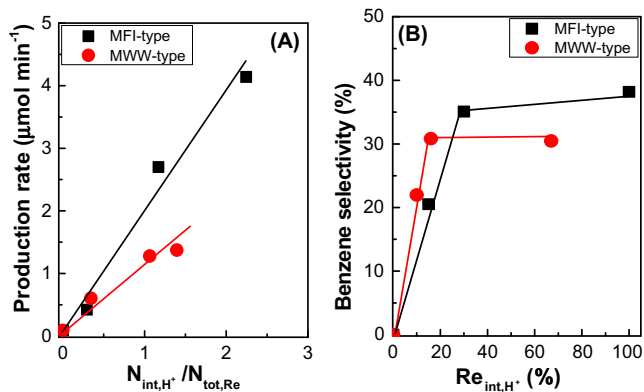


Fig. 10. (A) Product formation rate versus  $N_{\text{int,H}^+}/N_{\text{tot,Re}}$  ratio and (B) benzene product selectivity versus percentage of  $\text{Re}_{\text{int,H}^+}$  in DNMC reaction over both ReO<sub>x</sub>/MFI and ReO<sub>x</sub>/MWW catalysts. (Both product formation rate and selectivity are shown on the C-atom basis at the reaction time of 4.35 h).

characterizations on ReO<sub>x</sub>/zeolite samples indicates that ReO<sub>x</sub> species interacts with Brønsted acid sites of zeolites to form O<sub>2</sub>Re(μ-O<sub>2</sub>)ReO<sub>2</sub><sup>2+</sup> dimer or Si-O<sub>7</sub>ReO<sub>3</sub>-Al monomer structures. The increase in zeolite acidity favors the formation of O<sub>2</sub>Re(μ-O<sub>2</sub>)ReO<sub>2</sub><sup>2+</sup> dimer structure, as shown in Scheme 1. The linkage between the anchor-

ing structure of Re sites in zeolites and the benzene selectivity suggests that the cyclization of reaction intermediates for benzene formation in DNMC might primarily take place on the Si-O<sub>7</sub>ReO<sub>3</sub>-Al monomer structure. The increase in naphthalene selectivity on Re/MFI-15 than other catalysts samples in Fig. 9 and Fig. S1 (refer to supporting information) suggests that the O<sub>2</sub>Re(μ-O<sub>2</sub>)ReO<sub>2</sub><sup>2+</sup> dimer might favor further cyclization reaction for formation of heavy aromatics. Overall, the benzene formation seems to be dominated by the percentage of internal Re<sub>int,H<sup>+</sup></sub> monomer sites in ReO<sub>x</sub>/zeolite samples.

#### 4. Conclusions

The anchoring nature and spatial distribution of ReO<sub>x</sub> species in zeolite supports with various acidity and meso-/microporosity were studied. ReO<sub>x</sub> species were observed to resemble the isolated tetrahedral ReO<sub>4</sub><sup>-</sup> structure in zeolite supports and preferentially anchor onto Brønsted acid sites (Si-OH<sup>+</sup>-Al) of zeolite when the Si/Al ratio is low. The decrease in zeolite acidity (or increase in Si/Al ratio) results in the anchoring mode of ReO<sub>x</sub> species onto both Si-OH<sup>+</sup>-Al and silanol (Si-OH) groups. The presence of mesoporosity in zeolites (for example, 2D lamellar zeolites) enables a high concentration of Si-OH groups that act as sites for anchoring of ReO<sub>x</sub> species. The Brønsted acid site measurement by organic titra-

tion in combination with the DRIFTS measurement quantified the nearly one-to-one ratio (i.e.,  $H^+/Re$  ratio = 1.1) for replacement of protons in Si-OH<sup>+</sup>-Al sites by ReO<sub>x</sub> species in zeolite with high acidity, and presumably for samples with low acidity and/or mesoporosity. A quantitative correlation between loss of Si-OH groups and ReO<sub>x</sub> species was not found, but a significant loss of Si-OH groups in micro-/mesoporous 2D zeolites upon ReO<sub>x</sub> residence was confirmed. The implication of distribution of ReO<sub>x</sub> in zeolite was explored by direct non-oxidative methane conversion reaction. The present study provides a systematic fundamental understanding of structures of metal oxide/zeolite catalysts, particularly for zeolite supports with low acidity and mesoporosity.

## Acknowledgements

The authors gratefully acknowledge financial support from the National Science Foundation (NSF-CBET 1264599 and 1351384). We acknowledge the support of Maryland NanoCenter and its NispLab. The NispLab is supported in part by the NSF as a MRSEC Shared Experimental Facility. Yiqing Wu thanks for the Hulka Energy Research Fellowship from University of Maryland Energy Research Center (UMERC) to support this research. Scott Holdren also thanks the GAANN Fellowship program for financial support. Zheng Lu and Yu Lei thank the support from the American Chemical Society Petroleum Research Fund (ACS-PRF, 56197DNI5). MRCAT operations are supported by the Department of Energy and the MRCAT member institutions. This research used resources of the Advanced Photon Source, a U.S. Department of Energy (DOE) Office of Science User Facility operated for the DOE Office of Science by Argonne National Laboratory under Contract DEAC02-06CH11357.

## Appendix A. Supplementary material

Supplementary data to this article can be found online at <https://doi.org/10.1016/j.jcat.2019.02.024>.

## References

- [1] T. Barakat, J.C. Rooke, H.L. Tidahy, M. Hosseini, R. Cousin, J.F. Lamonier, J.M. Giraudon, G. De Weireld, B.L. Su, S. Siffert, Noble-metal-based catalysts supported on zeolites and macro-mesoporous metal oxide supports for the total oxidation of volatile organic compounds, *ChemSusChem* 4 (2011) 1420–1430, <https://doi.org/10.1002/cssc.201100282>.
- [2] D. Wang, D. Astruc, The recent development of efficient earth-abundant transition-metal nanocatalysts, *Chem. Soc. Rev.* 46 (2017) 816–854, <https://doi.org/10.1039/C6CS00629A>.
- [3] S. Lwin, I.E. Wachs, Olefin metathesis by supported metal oxide catalysts, *ACS Catal.* 4 (2014) 2505–2520, <https://doi.org/10.1021/cs500528h>.
- [4] L. Sandbrink, E. Klindworth, H.U. Islam, A.M. Beale, R. Palkovits, ReO<sub>x</sub>/TiO<sub>2</sub>: a recyclable solid catalyst for deoxydehydration, *ACS Catal.* 6 (2016) 677–680, <https://doi.org/10.1021/acscatal.5b01936>.
- [5] Z.R. Ismagilov, E.V. Matus, L.T. Tsikoza, Direct conversion of methane on Mo/ZSM-5 catalysts to produce benzene and hydrogen: achievements and perspectives, *Energy Environ. Sci.* 1 (2008) 526–541, <https://doi.org/10.1039/B810981H>.
- [6] N. Kosinov, F. Coumans, E.A. Uslamin, A.S.G. Wijpkema, B. Mezari, E.J.M. Hensen, Methane Dehydroaromatization by Mo/HZSM-5: mono- or bifunctional Catalysis?, *ACS Catal.* 7 (2017) 520–529, <https://doi.org/10.1021/acscatal.6b02497>.
- [7] H.Y. Kim, H.M. Lee, R.G.S. Pala, H. Metiu, Oxidative dehydrogenation of methanol to formaldehyde by isolated vanadium, molybdenum, and chromium oxide clusters supported on rutile TiO<sub>2</sub>(110), *J. Phys. Chem. C* 113 (2009) 16083–16093, <https://doi.org/10.1021/jp903298w>.
- [8] J.R. Sohn, S.G. Ryu, Redox and catalytic behaviors of chromium oxide supported on zirconia, *Catal. Lett.* 74 (2001) 105–110, <https://doi.org/10.1023/A:1016643232442>.
- [9] M. Stoyanova, U. Rodemerck, U. Bentrup, U. Dingerdissen, D. Linke, R.W. Mayer, H. Rotgerink, T. Tacke, High-throughput preparation and screening of rhenium oxide-alumina catalysts in olefin metathesis, *Appl. Catal. A-Gen.* 340 (2008) 242–249, <https://doi.org/10.1016/j.apcata.2008.02.017>.
- [10] H. Liu, E. Iglesia, Selective oxidation of methanol and ethanol on supported ruthenium oxide clusters at low temperatures, *J. Phys. Chem. B* 109 (2005) 2155–2163, <https://doi.org/10.1021/jp0401980>.
- [11] D.S. Kim, I.E. Wachs, Surface rhenium oxide-support interaction for supported Re2O7 catalysts, *J. Catal.* 141 (1993) 419–429, <https://doi.org/10.1006/jcat.1993.1151>.
- [12] B. Mitra, X.T. Gao, I.E. Wachs, A.M. Hirt, G. Deo, Characterization of supported rhenium oxide catalysts: effect of loading, support and additives, *Phys. Chem. Chem. Phys.* 3 (2001) 1144–1152, <https://doi.org/10.1039/B007381O>.
- [13] R.W. Borry, Y.H. Kim, A. Huffsmith, J.A. Reimer, E. Iglesia, Structure and density of Mo and acid sites in Mo-exchanged H-ZSM5 catalysts for nonoxidative methane conversion, *J. Phys. Chem. B* 103 (1999) 5787–5796, <https://doi.org/10.1021/jp990866v>.
- [14] W. Li, G.D. Meitzner, R.W. Borry, E. Iglesia, Raman and x-ray absorption studies of Mo species in Mo/H-ZSM5 catalysts for non-oxidative CH4 reactions, *J. Catal.* 191 (2000) 373–383, <https://doi.org/10.1006/jcat.1999.2795>.
- [15] J. Gao, Y.T. Zheng, J.M. Jehng, Y.D. Tang, I.E. Wachs, S.G. Podkolzin, Identification of molybdenum oxide nanostructures on zeolites for natural gas conversion, *Science* 348 (2015) 686–690, <https://doi.org/10.1126/science.aaa7048>.
- [16] Y.Q. Wu, L. Emdadi, S.C. Oh, M. Sakbodin, D.X. Liu, Spatial distribution and catalytic performance of metal-acid sites in Mo/MFI catalysts with tunable meso-/microporous lamellar zeolite structures, *J. Catal.* 323 (2015) 100–111, <https://doi.org/10.1016/j.jcat.2014.12.022>.
- [17] Y. Wu, L. Emdadi, Z. Wang, W. Fan, D. Liu, Textural and catalytic properties of Mo loaded hierarchical meso-/microporous lamellar MFI and MWW zeolites for direct methane conversion, *Appl. Catal. A-Gen.* 470 (2014) 344–354, <https://doi.org/10.1016/j.apcata.2013.10.053>.
- [18] H. Jahangiri, J. Bennett, P. Mahjoubi, K. Wilson, S. Gu, A review of advanced catalyst development for Fischer-Tropsch synthesis of hydrocarbons from biomass derived syn-gas, *Catal. Sci. Technol.* 4 (2014) 2210–2229, <https://doi.org/10.1039/C4CY00327F>.
- [19] L. Wang, J. Zhang, X. Yi, A. Zheng, F. Deng, C. Chen, Y. Ji, F. Liu, X. Meng, F.-S. Xiao, Mesoporous ZSM-5 zeolite-supported Ru nanoparticles as highly efficient catalysts for upgrading phenolic biomolecules, *ACS Catal.* 5 (2015) 2727–2734, <https://doi.org/10.1021/acscatal.5b00083>.
- [20] C. Zhao, Y. Kou, A.A. Lemomidou, X. Li, J.A. Lercher, Highly selective catalytic conversion of phenolic bio-oil to alkanes, *Angew. Chem. Int. Edit.* 48 (2009) 3987–3990, <https://doi.org/10.1002/anie.200900404>.
- [21] T. Yokoi, T. Tatsumi, Interlayer expansion of the layered zeolites, in: F.S. Xiao, X. Meng (Eds.), *Zeolites in Sustainable Chemistry*, Springer, Berlin, 2016, p. 77, [https://doi.org/10.1007/978-3-662-47395-5\\_3](https://doi.org/10.1007/978-3-662-47395-5_3).
- [22] B.Y. Liu, C. Wattanaprayoon, S.C. Oh, L. Emdadi, D.X. Liu, Synthesis of organic pillared MFI zeolite as bifunctional acid-base catalyst, *Chem. Mater.* 27 (2015) 1479–1487, <https://doi.org/10.1021/cm5033833>.
- [23] M. Mazur, P. Chlubna-Eliasova, W.J. Roth, J. Cejka, Intercalation chemistry of layered zeolite precursor IPC-1P, *Catal. Today* 227 (2014) 37–44, <https://doi.org/10.1016/j.cattod.2013.10.051>.
- [24] W.J. Roth, C.T. Kresge, Intercalation chemistry of NU-6(1), the layered precursor to zeolite NSL, leading to the pillared zeolite MCM-39(Si), *Micro. Meso. Mater.* 144 (2011) 158–161, <https://doi.org/10.1016/j.micromeso.2011.04.006>.
- [25] A. Corma, U. Diaz, T. Garcia, G. Sastre, A. Velty, Multifunctional hybrid organic-inorganic catalytic materials with a hierarchical system of well-defined micro- and mesopores, *J. Am. Chem. Soc.* 132 (2010) 15011–15021, <https://doi.org/10.1021/ja106272z>.
- [26] X.Y. Ouyang, S.J. Hwang, R.C. Runnebaum, D. Xie, Y.J. Wanglee, T. Rea, S.I. Zones, A. Katz, Single-step delamination of a MWW borosilicate layered zeolite precursor under mild conditions without surfactant and sonication, *J. Am. Chem. Soc.* 136 (2014) 1449–1461, <https://doi.org/10.1021/ja410141u>.
- [27] I. Ogino, E.A. Eilertsen, S.J. Hwang, T. Rea, D. Xie, X.Y. Ouyang, S.I. Zones, A. Katz, Heteroatom-tolerant delamination of layered zeolite precursor materials, *Chem. Mater.* 25 (2013) 1502–1509, <https://doi.org/10.1021/cm3032785>.
- [28] K. Varoon, X.Y. Zhang, B. Elyassi, D.D. Brewer, M. Gettel, S. Kumar, J.A. Lee, S. Maheshwari, A. Mittal, C.Y. Sung, M. Coccocioni, L.F. Francis, A.V. McCormick, K.A. Mkhoyan, M. Tsapatsis, Dispersible exfoliated zeolite nanosheets and their application as a selective membrane, *Science* 334 (2011) 72–75, <https://doi.org/10.1126/science.1208891>.
- [29] I. Ogino, M.M. Nigra, S.J. Hwang, J.M. Ha, T. Rea, S.I. Zones, A. Katz, Delamination of layered zeolite precursors under mild conditions: synthesis of UCB-1 via fluoride/chloride anion-promoted exfoliation, *J. Am. Chem. Soc.* 133 (2011) 3288–3291, <https://doi.org/10.1021/ja111147z>.
- [30] A. Corma, V. Fornes, S.B. Pergher, T.L.M. Maesen, J.G. Buglass, Delaminated zeolite precursors as selective acidic catalysts, *Nature* 396 (1998) 353–356, <https://doi.org/10.1038/24592>.
- [31] K. Na, M. Choi, W. Park, Y. Sakamoto, O. Terasaki, R. Ryoo, Pillared MFI zeolite nanosheets of a single-unit-cell thickness, *J. Am. Chem. Soc.* 132 (2010) 4169–4177, <https://doi.org/10.1021/ja908382n>.
- [32] S. Maheshwari, E. Jordan, S. Kumar, F.S. Bates, R.L. Penn, D.F. Shantz, M. Tsapatsis, Layer structure preservation during swelling, pillaring, and exfoliation of a zeolite precursor, *J. Am. Chem. Soc.* 130 (2008) 1507–1516, <https://doi.org/10.1021/ja077711i>.
- [33] J. Gao, Y.T. Zheng, Y.D. Tang, J.M. Jehng, R. Grybos, J. Handzlik, I.E. Wachs, S.G. Podkolzin, Spectroscopic and Computational Study of Cr Oxide Structures and Their Anchoring Sites on ZSM-5 Zeolites, *ACS Catal.* 5 (2015) 3078–3092, <https://doi.org/10.1021/acscatal.5b00333>.
- [34] J. Gao, Y.T. Zheng, G.B. Fitzgerald, J. de Joannis, Y.D. Tang, I.E. Wachs, S.G. Podkolzin, Structure of Mo2Cx and Mo4Cx, molybdenum carbide nanoparticles and their anchoring sites on ZSM-5 zeolites, *J. Phys. Chem. C* 118 (2014) 4670–4679, <https://doi.org/10.1021/jp4106053>.

- [35] P. Cheung, A. Bhan, G.J. Sunley, D.J. Law, E. Iglesia, Site requirements and elementary steps in dimethyl ether carbonylation catalyzed by acidic zeolites, *J. Catal.* 245 (2007) 110–123, <https://doi.org/10.1016/j.jcat.2006.09.020>.
- [36] P. Cheung, A. Bhan, G.J. Sunley, E. Iglesia, Selective carbonylation of dimethyl ether to methyl acetate catalyzed by acidic zeolites, *Angew. Chem. Int. Edit.* 45 (2006) 1617–1620, <https://doi.org/10.1002/anie.200503898>.
- [37] D. Liu, A. Bhan, M. Tsapatsis, S. Al, Hashimi, *Catalytic behavior of Brønsted acid sites in MWW and MFI zeolites with dual meso- and microporosity*, *ACS, Catal.* 1 (2011) 7–17, <https://doi.org/10.1021/cs100042r>.
- [38] S. Lwin, C. Keturakis, J. Handzlik, P. Sautet, Y.Y. Li, A.I. Frenkel, I.E. Wachs, Surface ReOx sites on Al<sub>2</sub>O<sub>3</sub> and their molecular structure reactivity relationships for olefin metathesis, *ACS, Catal.* 5 (2015) 1432–1444, <https://doi.org/10.1021/cs5016518>.
- [39] S. Lwin, Y.Y. Li, A.I. Frenkel, I.E. Wachs, Activation of surface ReOx sites on Al<sub>2</sub>O<sub>3</sub> catalysts for olefin metathesis, *ACS, Catal.* 5 (2015) 6807–6814, <https://doi.org/10.1021/acscatal.5b01944>.
- [40] S. Lwin, I.E. Wachs, Determination of number of activated sites present during olefin metathesis by supported ReOx/Al<sub>2</sub>O<sub>3</sub> catalysts, *ACS, Catal.* 5 (2015) 6823–6827, <https://doi.org/10.1021/acscatal.5b01597>.
- [41] T. Kusakari, T. Sasaki, Y. Iwasawa, Selective oxidation of benzene to phenol with molecular oxygen on rhenium/zeolite catalysts, *Chem. Comm.* (2004) 992–993, <https://doi.org/10.1039/B401373E>.
- [42] R. Bal, M. Tada, T. Sasaki, Y. Iwasawa, Direct phenol synthesis by selective oxidation of benzene with molecular oxygen on an interstitial-N/Re cluster/zeolite catalyst, *Angew. Chem. Int. Edit.* 45 (2006) 448–452, <https://doi.org/10.1002/anie.200502940>.
- [43] L. Wang, S. Yamamoto, S. Malwadkar, S.-I. Nagamatsu, T. Sasaki, K. Hayashizaki, M. Tada, Y. Iwasawa, Direct synthesis of phenol from benzene and O<sub>2</sub>, regulated by NH<sub>3</sub> on Pt/β and Pt-Re/ZSM-5 catalysts, *Chemcatchem* 5 (2013) 2203–2206, <https://doi.org/10.1002/cctc.201300166>.
- [44] J.M. Serra, E. Guillon, A. Corma, Optimizing the conversion of heavy reformat streams into xylenes with zeolite catalysts by using knowledge base high-throughput experimentation techniques, *J. Catal.* 232 (2005) 342–354, <https://doi.org/10.1016/j.jcat.2005.03.021>.
- [45] D. Mandelli, M.C.A. van Vliet, U. Arnold, R.A. Sheldon, U. Schuchardt, Epoxidation of alkenes with hydrogen peroxide catalyzed by ReO<sub>4</sub>-SiO<sub>2</sub> center dot Al<sub>2</sub>O<sub>3</sub> and ReO<sub>4</sub>-Al<sub>2</sub>O<sub>3</sub>, *J. Mol. Catal. A-Chem.* 168 (2001) 165–171, [https://doi.org/10.1016/S1381-1169\(00\)00521-5](https://doi.org/10.1016/S1381-1169(00)00521-5).
- [46] H.S. Lacheen, P.J. Cordeiro, E. Iglesia, Structure and catalytic function of Re-oxo species grafted onto H-MFI zeolite by sublimation of Re<sub>2</sub>O<sub>7</sub>, *J. Am. Chem. Soc.* 128 (2006) 15082–15083, <https://doi.org/10.1021/ja065832x>.
- [47] H.S. Lacheen, P.J. Cordeiro, E. Iglesia, Isolation of rhenium and ReOx species within ZSM5 channels and their catalytic function in the activation of alkanes and alkanols, *Chem-Eur J.* 13 (2007) 3048–3057, <https://doi.org/10.1002/chem.200601602>.
- [48] J.O. Barth, A. Jentys, J. Kornatowski, J.A. Lercher, Control of acid-base properties of new nanocomposite derivatives of MCM-36 by mixed oxide pillaring, *Chem. Mater.* 16 (2004) 724–730, <https://doi.org/10.1021/cm0349607>.
- [49] M. Choi, K. Na, J. Kim, Y. Sakamoto, O. Terasaki, R. Ryoo, Stable single-unit-cell nanosheets of zeolite MFI as active and long-lived catalysts, *Nature* 461 (2009) 246–U120, <https://doi.org/10.1038/nature08288>.
- [50] L. Emdadi, Y.Q. Wu, G.H. Zhu, C.C. Chang, W. Fan, T. Pham, R.F. Lobo, D.X. Liu, Dual template synthesis of meso- and microporous MFI zeolite nanosheet assemblies with tailored activity in catalytic reactions, *Chem. Mater.* 26 (2014) 1345–1355, <https://doi.org/10.1021/cm401119d>.
- [51] X. Zhang, D. Liu, D. Xu, S. Asahina, K.A. Cychosz, K.V. Agrawal, Y. Al Wahedi, A. Bhan, S. Al Hashimi, O. Terasaki, M. Thommes, M. Tsapatsis, Synthesis of self-pillared zeolite nanosheets by repetitive branching, *Science* 336 (2012) 1684–1687, <https://doi.org/10.1126/science.1221111>.
- [52] D. Liu, X. Zhang, A. Bhan, M. Tsapatsis, Activity and selectivity differences of external Brønsted acid sites of single-unit-cell thick and conventional MFI and MWW zeolites, *Micro. Meso. Mater.* 200 (2014) 287–290, <https://doi.org/10.1016/j.micromeso.2014.06.029>.
- [53] S.C. Oh, T. Nguyen, Y. He, A. Filie, Y. Wu, D.T. Tran, I.C. Lee, D. Liu, External surface and pore mouth catalysis in hydrolysis of inulin over zeolites with different micropore topologies and mesoporosities, *Catal. Sci. Technol.* 7 (2017) 1153–1166, <https://doi.org/10.1039/C6CY02613C>.
- [54] Y. He, T.C. Hoff, L. Emdadi, Y. Wu, J. Bouraima, D. Liu, Catalytic consequences of micropore topology, mesoporosity, and acidity on the hydrolysis of sucrose over zeolite catalysts, *Catal. Sci. Technol.* 4 (2014) 3064–3073, <https://doi.org/10.1039/C4CY00360H>.
- [55] J. Zhang, Z. Lu, W. Wu, D.T. Tran, W. Shang, H. Chen, Y. Lei, Z. Li, M. Wang, T.J. Woehl, D. Liu, Mesopore differences between pillared lamellar MFI and MWW zeolites probed by atomic layer deposition of titania and consequences on photocatalysis, *Micro. Meso. Mater.* 276 (2019) 260–269, <https://doi.org/10.1016/j.micromeso.2018.10.009>.
- [56] P.K. Dutta, M. Puri, Synthesis and structure of zeolite ZSM-5 - a Raman-spectroscopic study, *J. Phys. Chem.-Us* 91 (1987) 4329–4333, <https://doi.org/10.1021/j100300a025>.
- [57] P. McMillan, Structural studies of silicate glasses and melts-applications and limitations of Raman spectroscopy, *Am. Mineral.* 69 (1984) 622–644.
- [58] E.L. Lee, I.E. Wachs, In situ Raman spectroscopy of SiO<sub>2</sub>-supported transition metal oxide catalysts: An isotopic O-18–O-16 exchange study, *J. Phys. Chem. C* 112 (2008) 6487–6498, <https://doi.org/10.1021/jp076485w>.
- [59] E.L. Lee, I.E. Wachs, In situ spectroscopic investigation of the molecular and electronic structures of SiO<sub>2</sub> supported surface metal oxides, *J. Phys. Chem. C* 111 (2007) 14410–14425, <https://doi.org/10.1021/jp0735482>.
- [60] X.T. Gao, S.R. Bare, B.M. Weckhuysen, I.E. Wachs, In situ spectroscopic investigation of molecular structures of highly dispersed vanadium oxide on silica under various conditions, *J. Phys. Chem. B* 102 (1998) 10842–10852, <https://doi.org/10.1021/jp9826367>.
- [61] F.P.J.M. Kerkhof, J.A. Moulijn, R. Thomas, Laser-Raman spectroscopy of the alumina-supported rhenium oxide metathesis catalyst, *J. Catal.* 56 (1979) 279–283, [https://doi.org/10.1016/0021-9517\(79\)90115-5](https://doi.org/10.1016/0021-9517(79)90115-5).
- [62] R.M. Edeva-Kardjjeva, A.A. Andreev, Formation and structure of the Re<sub>2</sub>O<sub>7</sub>-γ-Al<sub>2</sub>O<sub>3</sub> system under pre-catalysis conditions, *J. Catal.* 94 (1985) 97–107, [https://doi.org/10.1016/0021-9517\(85\)90085-5](https://doi.org/10.1016/0021-9517(85)90085-5).
- [63] F.D. Hardcastle, I.E. Wachs, J.A. Horsley, G.H. Via, The structure of surface rhenium oxide on alumina from laser Raman-spectroscopy and x-ray absorption near-edge spectroscopy, *J. Mol. Catal.* 46 (1988) 15–36, [https://doi.org/10.1016/0304-5102\(88\)85081-8](https://doi.org/10.1016/0304-5102(88)85081-8).
- [64] F. Schekler-Nahama, O. Clause, D. Commereuc, J. Saussey, Evidences for the presence of aluminium perchlenate at the surface of Re<sub>2</sub>O<sub>7</sub>/Al<sub>2</sub>O<sub>3</sub> metathesis catalysts, *Appl. Catal. A-Gen.* 167 (1998) 247–256, [https://doi.org/10.1016/S0926-860X\(97\)00311-6](https://doi.org/10.1016/S0926-860X(97)00311-6).
- [65] Y. Yuan, T. Shido, Y. Iwasawa, The new catalytic property of supported rhenium oxides for selective oxidation of methanol to methylal, *Chem. Comm.* (2000) 1421–1422, <https://doi.org/10.1039/B003870J>.
- [66] B.C. Vicente, R.C. Nelson, A.W. Moses, S. Chattopadhyay, S.L. Scott, Interactions involving Lewis acidic aluminum sites in oxide-supported perchlenate catalysts, *J. Phys. Chem. C* 115 (2011) 9012–9024, <https://doi.org/10.1021/jp109929g>.
- [67] Y. Kon, M. Araque, T. Nakashima, S. Paul, F. Dumeignil, B. Katryniok, Direct conversion of glycerol to allyl alcohol over alumina-supported rhenium oxide, *Chem. Sel.* 2 (2017) 9864–9868, <https://doi.org/10.1002/slct.201702070>.
- [68] Y. Yu, G. Xiong, C. Li, F.S. Xiao, Characterization of aluminosilicate zeolites by UV Raman spectroscopy, *Micro. Meso. Mater.* 46 (2001) 23–34, [https://doi.org/10.1016/S1387-1811\(01\)00271-2](https://doi.org/10.1016/S1387-1811(01)00271-2).
- [69] L.S. Wang, R. Ohnishi, M. Ichikawa, Selective dehydroaromatization of methane toward benzene on Re/HZSM-5 catalysts and effects of CO/CO<sub>2</sub> addition, *J. Catal.* 190 (2000) 276–283, <https://doi.org/10.1006/jcat.1999.2748>.
- [70] J. Macht, C.D. Baertsch, M. May-Lozano, S.L. Soled, Y. Wang, E. Iglesia, Support effects on Brønsted acid site densities and alcohol dehydration turnover rates on tungsten oxide domains, *J. Catal.* 227 (2004) 479–491, <https://doi.org/10.1016/j.jcat.2004.08.014>.
- [71] D. Fărcașiu, R. Leu, A. Corma, Evaluation of accessible acid sites on solids by 15N NMR spectroscopy with di-tert-butylpyridine as base, *J. Phys. Chem. B* 106 (2002) 928–932, <https://doi.org/10.1021/jp012221c>.
- [72] Y. Wu, L. Emdadi, D. Qin, J. Zhang, D. Liu, Quantification of external surface and pore mouth acid sites in unit-cell thick pillared MFI and pillared MWW zeolites, *Micro. Meso. Mater.* 241 (2017) 43–51, <https://doi.org/10.1016/j.micromeso.2016.12.004>.
- [73] S.-H. Park, H.-K. Rhee, Shape selective properties of MCM-22 catalysts for the disproportionation of ethylbenzene, *Appl. Catal. A-Gen.* 219 (2001) 99–105, [https://doi.org/10.1016/S0926-860X\(01\)00671-8](https://doi.org/10.1016/S0926-860X(01)00671-8).
- [74] A. Corma, V. Fornes, L. Forni, F. Marquez, J. Martinez-Triguero, D. Moscotti, 2,6-di-tert-butyl-pyridine as a probe molecule to measure external acidity of zeolites, *J. Catal.* 179 (1998) 451–458, <https://doi.org/10.1006/jcat.1998.2233>.
- [75] N. Viswanadham, T. Shido, Y. Iwasawa, Performances of rhenium oxide-encapsulated ZSM-5 catalysts in propene selective oxidation/ammoxidation, *Appl. Catal. A-Gen.* 219 (2001) 223–233, [https://doi.org/10.1016/S0926-860X\(01\)00695-0](https://doi.org/10.1016/S0926-860X(01)00695-0).
- [76] P. Bräuer, P.L. Ng, O. Situmorang, I. Hitchcock, C. D'Agostino, Effect of Al content on number and location of hydroxyl acid species in zeolites: a DRIFTS quantitative protocol without the need for molar extinction coefficients, *RSC Adv.* 7 (2017) 52604–52613, <https://doi.org/10.1039/C7RA10699H>.
- [77] P. Bräuer, O. Situmorang, P.L. Ng, C. D'Agostino, Effect of Al content on the strength of terminal silanol species in ZSM-5 zeolite catalysts: a quantitative DRIFTS study without the use of molar extinction coefficients, *Phys. Chem. Chem. Phys.* 20 (2018) 4250–4262, <https://doi.org/10.1039/C7CP07826A>.
- [78] R. Wei, H. Yang, J.A. Scott, K.-F. Aguey-Zinsou, D. Zhang, Synthesis of 2D MFI zeolites in the form of self-interlocked nanosheet stacks with tuneable structural and chemical properties for catalysis, *Appl. Mater. Today* 11 (2018) 22–33, <https://doi.org/10.1016/j.apmt.2018.01.007>.
- [79] A. Platon, W.J. Thomson, Quantitative Lewis/Brønsted ratios using DRIFTS, *Ind. Eng. Chem. Res.* 42 (2003) 5988–5992, <https://doi.org/10.1021/ie030343g>.
- [80] S.H. Kwak, *Spectroscopic characterization of the surface hydroxyls of zeolitic catalysts*, in: *Mathematics and Natural Sciences*, UNIVERSITY OF OSLO, 2014, p. 174.
- [81] V.B. Kazansky, A.I. Serykh, V. Semmer-Herledan, J. Fraissard, Intensities of OH IR stretching bands as a measure of the intrinsic acidity of bridging hydroxyl groups in zeolites, *Phys. Chem. Chem. Phys.* 5 (2003) 966–969, <https://doi.org/10.1039/B212331M>.